Geophysical Journal International

Geophys. J. Int. (2023) **233,** 1036–1054
Advance Access publication 2022 December 15
GJI Seismology

https://doi.org/10.1093/gji/ggac494

Bayesian regional moment tensor from ocean bottom seismograms recorded in the Lesser Antilles: implications for regional stress field

Mike Lindner,[1] Andreas Rietbrock,[1] Lidong Bie,[2] Saskia Goes,[3] Jenny Collier,[3] Catherine Rychert,[4] Nicholas Harmon,[4] Stephen P. Hicks,[3] Tim Henstock[4] and the VoiLA working group

[1] *Geophysical Institute (GPI), Karlsruhe Institute of Technology,* 76131 *Karlsruhe, Germany. E-mail: mike.lindner@kit.edu*
[2] *School of Environmental Sciences, University of East Anglia, Norwich Research Park, Norwich NR*4 7*TJ, United Kingdom*
[3] *Department of Earth Sciences and Engineering, Imperial College London, South Kensington, London SW*7 2*BX, United Kingdom*
[4] *Ocean and Earth Science, National Oceanography Centre Southampton, University of Southampton, Southampton SO*17 1*BJ, United Kingdom*

Accepted 2022 December 16. Received 2022 December 5; in original form 2022 May 10

SUMMARY

Seismic activity in the Lesser Antilles (LA) is characterized by strong regional variability along the arc reflecting the complex subduction setting and history. Although routine seismicity monitoring can rely on an increasing number of island stations, the island-arc setting means that high-resolution monitoring and detailed studies of fault structures require a network of ocean bottom seismometers (OBS). As part of the 2016–2017 **Vo**lat**i**le recycling at the **L**esser **A**ntilles arc (VoiLA) project, we deployed 34 OBS stations in the forearc and backarc. During the deployment time, 381 events were recorded within the subduction zone. In this paper, we perform full-waveform regional moment tensor (RMT) inversions, to gain insight into the stress distribution along the arc and at depth. We developed a novel inversion approach, AmΦB—'Amphibious Bayesian', taking into account uncertainties associated with OBS deployments. Particularly, the orientation of horizontal components (alignment uncertainty) and the high noise level on them due to ocean microseisms are accounted for using AmΦB. The inversion is conducted using a direct, uniform importance sampling of the fault parameters within a multidimensional tree structure: the uniXtree-sampling algorithm. We show that the alignment of the horizontal OBS components, particularly in high noise level marine environments, influences the obtained source mechanism when using standard least-squares (L2) RMT inversion schemes, resulting in systematic errors in the recovered focal mechanisms including high artificial compensated linear vector dipole (CLVD) contributions. Our Bayesian formulation in AmΦB reduces these CLVD components by nearly 60 per cent and the aberration of the focal geometry as measured by the Kagan angle by around 40 per cent relative to a standard L2 inversion. Subsequently, we use AmΦB-RMT to obtain 45 (M_w > 3.8) regional MT solutions, out of which 39 are new to any existing database. Combining our new results with existing solutions, we subsequently analyse a total of 151 solutions in a focal mechanism classification (FMC) diagram and map them to the regional tectonic setting. We also use our newly compiled RMT database to perform stress tensor inversions along the LA subduction zone. On the plate interface, we observe the typical compressional stress regime of a subduction zone and find evidence for upper-plate strike slip and normal fault behaviour in the north that becomes a near arc-perpendicular extensional stress regime towards the south. A dominant slab perpendicular extensional stress regime is found in the slab at 100–200 km beneath the central part of the arc. We interpret this stress condition to be a result of slab pull varying along the arc due to partial slab detachment along previously hypothesized lateral slab tear near Grenada, at the southern end of the LA arc, leading to reactivation of pre-existing structures around the subducted Proto-Caribbean ridge.

See full list of VoiLA working group members at: http://www.voila.ac.uk/index.php/project_participants/.

Key words: Earthquake source observations; Seismicity and tectonics; Waveform inversion; Fractures, faults and high strain deformation zones; Subduction zone processes.

1 INTRODUCTION

The Lesser Antilles (LA) island arc (Fig. 1), located along the eastern margin of the Caribbean Sea, is part of a small yet highly complex subduction zone system that is driven by southwestward motions of the conjoined North and South American plates (Bouysse *et al.* 1990; Harris *et al.* 2018; Allen *et al.* 2019). Regional seismicity strongly varies along the arc (Hayes *et al.* 2013; Schlaphorst *et al.* 2016; Bie *et al.* 2020). The incoming oceanic plate is marked by large bathymetric structures north of 15°N that significantly affect the activity within the shallow forearc. These prominent structures are the Barracuda Ridge entering the trench at around 16.75°N and the Tiburon Rise around 15.25°N (Laigle *et al.* 2013a). Earthquake activity follows the outline of the arc and reaches down to a maximum depth of ∼190 km around the island of Martinique. To the north of Martinique at ∼14.5°N, the seismicity rate is highest, especially for events with a magnitude greater than 5, whereas to the south, between St Lucia and Grenada, an area with a much lower seismicity rate can be found. Even further south, seismic activity increases again near Tobago.

Recent studies (e.g. Ruiz *et al.* 2013; Laigle *et al.* 2013b, a; Gonzalez *et al.* 2017; Paulatto *et al.* 2017) focus mostly on the seismically active northern part of the LA arc between 14.5°N and 18.5°N. The main structural features of the subducted slab in this part of the arc include three prominent fracture zones, that is the 15–20, Marathon, and Mercurius (e.g. Harmon *et al.* 2019) and a domain boundary that separates plate material formed along the Proto-Caribbean and Equatorial Atlantic ridges (Cooper *et al.* 2020; Braszus *et al.* 2021). Although the exact orientations of these structures at depth are debated, the surface projections of the Marathon and Mercurius fracture zones and the domain boundary pass through the arc near Guadeloupe and Dominica, close to where the highest seismicity rate is also observed.

Since 1952, when regional instrumental earthquake recording started, the arc has been covered by internationally operated permanent stations overseen by the University of the West Indies (Seismic Research Center Trinidad): the current *TRN* Network consists of over 50 seismic stations covering the whole arc with further individual stations and local networks (e.g. CU, G, MQ, WI, etc.) from various agencies (e.g. IPGP, KNMI, USGS, etc.). The established extensive island instrumentation helped to significantly improve the regional earthquake data catalogue over the years.

Earthquake focal mechanisms (FMs) provide valuable insights into seismic fault structures and regional stress fields. However, no routine operational catalogue of focal mechanisms for the region exists. Available catalogues are based on retrospective, time-limited studies. Until 2021, to our knowledge, around 106 focal solutions of various quality were available for the northern part of the arc. Using local island stations, Gonzalez *et al.* (2017) derived 29 solutions using available waveforms of land stations. Ruiz *et al.* (2013) derived 22 focal mechanisms using first motion polarities from a temporal amphibious ocean-bottom seismic (OBS) experiment in the forearc offshore Dominica. The remaining solutions are from various international agencies (e.g. GCMT, Geofone and USGS), and are constrained by recordings at teleseismic distances.

Due to the shape of the LA island arc, regional land installations are restricted. This inherent coverage may bias the source mechanism solutions using land station data alone. An offshore extension of the local network is therefore essential to increase the database of regional FMs, particularly for small and intermediate-sized events. Compared to scarce large events with a magnitude greater than 7, more regularly occurring smaller events provide detailed insight into fault structures in the crust and the subducting Atlantic lithosphere. They also offer a chance to study the regional stress field and its variation along and across the arc.

Research projects investigating the physical properties of subduction zones now often incorporate OBS stations (e.g. Romanowicz *et al.* 1998; Ruiz *et al.* 2013; Cabieces *et al.* 2020; León-Ríos *et al.* 2021). However, the recorded data often provide only a limited source of information for regional moment tensor (RMT) source modelling, for example polarity information in a joined RMT inversion (e.g. Ruiz *et al.* 2013; Cabieces *et al.* 2020) or in an inversion restricted to pure double-couple solutions. Two main sources of errors may affect the effective incorporation of OBS data in RMT full-waveform inversions—one are ocean microseisms of which the dominant frequencies around 1.0–0.05 Hz (Yang *et al.* 2012) have a strong influence on the horizontal components of OBS stations (Fig. 2). The other source of error is the uncertainty in station locations and alignments of the sensors. Station locations have been assessed using direct arrival times and remaining uncertainties can be accepted if the recorded data are used for studies with wavelengths exceeding them. The influence of alignment, however, is frequency independent and directly affects waveform modelling analyses. Different methods have been developed to estimate the alignment angle of sensors relative to north, including ambient noise correlation (Zha *et al.* 2013), receiver functions (Janiszewski & Abers 2015; Lim *et al.* 2017), *P*-wave polarity (Wang *et al.* 2016) and its combination with Rayleigh-wave polarization (Doran & Laske 2017) using natural sources or even artificial ones like ship tracking (Trabattoni *et al.* 2020).

Existing RMT inversion routines can handle uncertainties related to the specific requirements of OBS deployments which are (i) the increased noise level of the observations (e.g. Duputel *et al.* 2012; Pugh *et al.* 2016; Vackář *et al.* 2017; Vasyura-Bathke *et al.* 2020), (ii) uncertainties in the source localization (Duputel *et al.* 2012) and (iii) the timing uncertainties in respect to the 1-D model, for example Cut-and-Paste (Zhao & Helmberger 1994). However, to our knowledge, none of these published approaches simultaneously consider the alignment uncertainty at an arbitrary station. Here we present a new inversion routine, AmΦB—Amphibious Bayesian, based on full waveform inversion (Krizova *et al.* 2013) in a Bayesian framework (Duputel *et al.* 2012). We introduce two covariance matrices—one for data error C_d associated with increased ambient noise and the second for the model error C_T as a function of the sensor alignment uncertainty. The inverse problem (e.g. Yagi & Fukahata 2008; Duputel *et al.* 2012) is then solved in a uniform tree-sampling search algorithm (Lomax & Curtis 2001), using the uniform Tape parametrization (Tape & Tape 2015) for a deviatoric source mechanism. Other sources of theoretical error can be caused by an uncertain velocity model (Duputel *et al.* 2014), errors in the hypocentre location (Duputel *et al.* 2012) or the source–time function (Staehler & Sigloch 2014). While we will not examine their effects on our RMT results in particular, potential effects will be discussed.

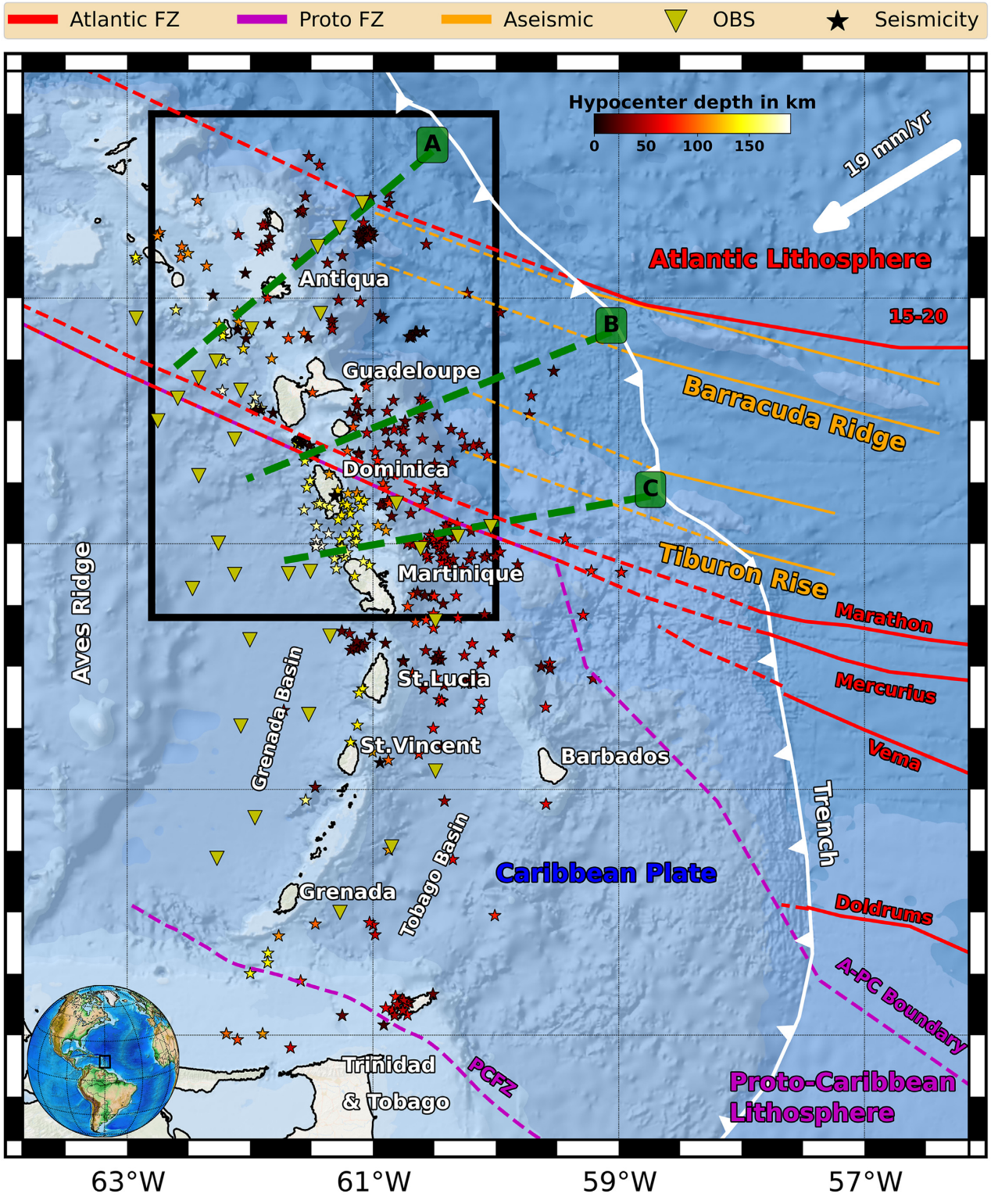

Figure 1. Bathymetric map of the Lesser Antilles subduction zone. The black box outlines the target area of this study. Triangles show the locations of the VoiLA OBS network, consisting of 32 broad-band stations, within the forearc and backarc region. Prominent fracture zones on the Atlantic lithosphere are marked in red, aseismics in orange and inferred features of the Proto-Caribbean lithosphere are marked in magenta. The dashed lines show the projected positions of these features along the subducted slab. Three cross-sections (A–C) are marked as green dotted lines. Background seismicity (black stars) during the operational time is taken from (Bie *et al.* 2020).

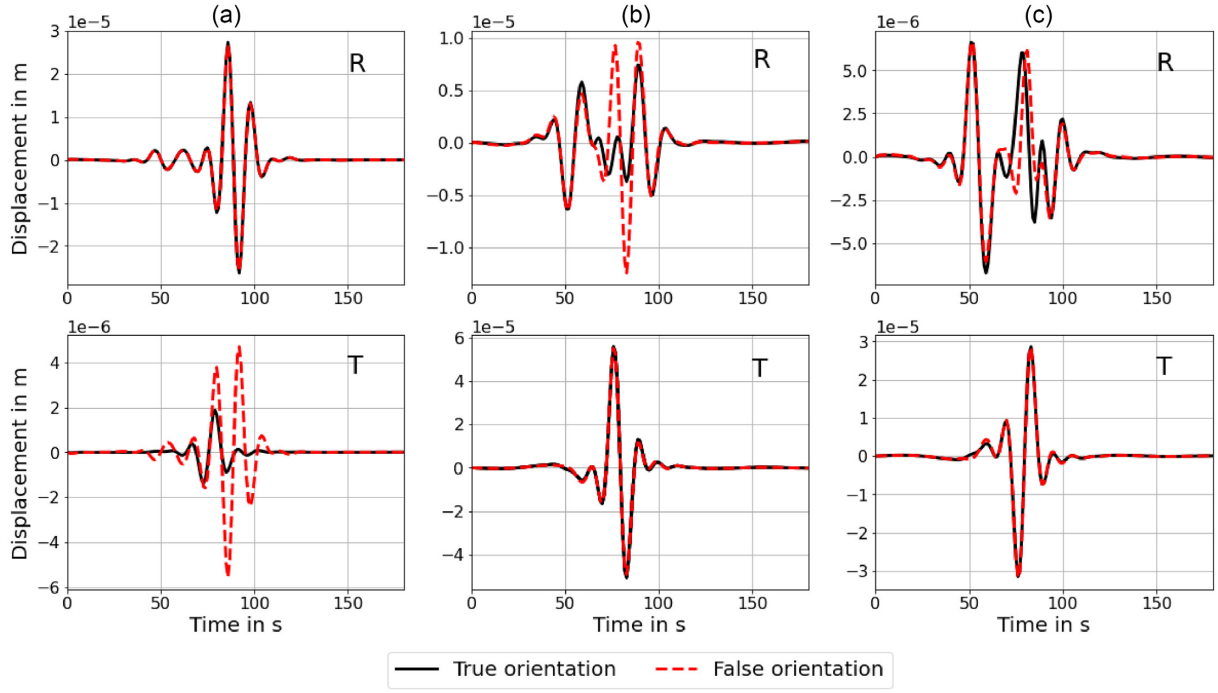

Figure 2. Probabilistic power spectral density (PPSD) at stations DP06 (a–c) and SI02 (d–f) computed for a total of 250 d of continuous data records in 2016.

In this study, we first demonstrate the effects of horizontal alignment uncertainties resulting from both error sources, using synthetic tests of two distinct focal solutions. Following these examinations, we apply our new RMT inversion routine to 45 events in the local earthquake catalogue (Bie *et al.* 2020). We then compile an RMT database that includes newly derived and pre-existing focal mechanism solutions for the northern part of the LA subduction zone and conduct an inversion for the regional stress orientations.

2 METHOD AmΦB—FULL WAVEFORM RMT INVERSION ROUTINE

An earthquake can be approximated mathematically as a point source by a symmetric second order moment tensor, which consists of six equivalent force couples (Aki & Richards 2002). The displacement time-series $d_j^{obs}(t)$ with $j \in [Z, R, T]$ recorded at a surface station is not only governed by the source mechanism but also the structural and material properties between source (earthquake) and receivers (seismic stations) (Jost & Herrmann 1989). The structural model provides a set of Green's functions G_{ij} that subsequently construct the synthetic displacement time-series in a linear weighted summation of the modelling elements m_i (e.g. moment tensor elements)

$$d_j^{obs}(t) = S(t) \cdot \sum_i^I G_{ij} \cdot m_i + e(t) \tag{1}$$

with source–time function $S(t)$ and residual $e(t)$. Design of $\mathbf{G}$ and model vector $\mathbf{m}$ is dependent on the number $i \in I$ of fundamental mechanisms the source is decomposed into (e.g. Zhao & Helmberger 1994; Krizova *et al.* 2013; Dahm & Krüger 2014). The radial symmetry of a 1-D velocity model requires only three pure double couple mechanisms to describe any arbitrary double couple source. Hereby, $\mathbf{G}$ is designed for displacement traces along pressure, tension and nodal axis, and assembled by incorporating the station azimuth as an additional parameter to the double couple source mechanism defined by strike, dip and rake (Zhao & Helmberger 1994). A full deviatoric model, on the other hand, is more sophisticated (Krizova *et al.* 2013) and uses five fundamental double-couple (DC) mechanisms at the given source–receiver geometry (e.g. Sokos & Zahradnik 2008, 2013; Zhu & Ben-Zion 2013). In the scope of this study we use a combination of both methods for a deviatoric source inversion. eq. (1) can be written in matrix form

$$d^{obs} = \mathbf{G}\mathbf{m} + E, \tag{2}$$

where the source–time function $S(t)$ from eq. (1) is integrated into the Green's function matrix. The error E is introduced to compensate differences between the synthetics and actual observation and has been used to comprise multiple uncertainties including source specific assumptions such as wrong centroid location (Duputel *et al.* 2012), variations in source–time function (Staehler & Sigloch 2014), fault structure complexities (Yagi & Fukahata 2008), station alignments (this study) or general local background noise (this study). Considering these uncertainties in the moment tensor inversion problem, eq. (2) can be expressed in an ordinary least squares formulation (e.g. Yagi & Fukahata 2008):

$$\left(\mathbf{G}\mathbf{m} - d^{\text{obs}}\right)^T \mathbf{C}_D^{-1} \left(\mathbf{G}\mathbf{m} - d^{\text{obs}}\right) \rightarrow \min. \tag{3}$$

To statistically quantify the errors, we introduce a Gaussian distributed probability density. We construct the probability density function (PDF) as stochastic information of the model space:

$$Q(\mathbf{m}) = k e^{-0.5[(\mathbf{G}\mathbf{m}-d^{\text{obs}})^T \mathbf{C}_D^{-1} (\mathbf{G}\mathbf{m}-d^{\text{obs}})]}, \tag{4}$$

where k is a normalization factor satisfying $\sum Q(\mathbf{m}) = 1$. Here, $\mathbf{C}_D$ represents the covariance matrix of error sum E. Likewise, this matrix can be decomposed into the underlying error sources following the error propagation rule

$$\mathbf{C}_D = \mathbf{C}_d + \mathbf{C}_T. \tag{5}$$

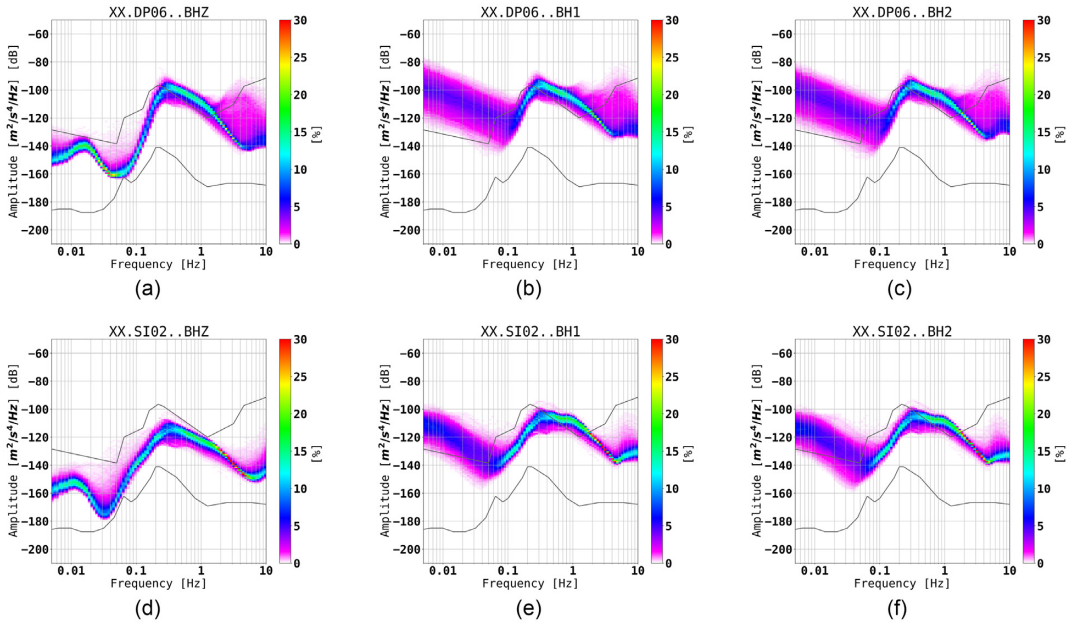

Figure 3. Influence of $d\Phi = 10^\circ$ station alignments of horizontal recordings for different source mechanism and station azimuth θ from a synthetic test. R = Radial; T = Transverse component. (a) Dip-Slip $(\psi, \theta, \lambda) = (0, 90, 90)$, $\theta = 80^\circ$ near p-axis (90°), energy on T gets minimal (b) Strike-Slip $(\psi, \theta, \lambda) = (0, 90, 0)$, $\theta = 20^\circ$ near n-axis (0°), energy on R gets minimal (c) Normal Fault $(\psi, \theta, \lambda) = (0, 45, -90)$, $\theta = 30^\circ$ near p-axis (45°), energy on R gets minimal.

We assume that error E is attributed to the two largest contributions for an OBS deployment: Ambient noise of ocean microseism with data covariance $\mathbf{C}_d$ and station dependent alignment of horizontal components defining model covariance matrix $\mathbf{C}_T$.

2.1 Ambient Noise

While land stations might have to deal with strong noise due to human activities inducing frequencies greater than 1 Hz (e.g. Lecocq *et al.* 2020), OBS stations are comparably quiet in this range (Yang *et al.* 2012). Instead, OBS recordings show a much stronger ocean-induced microseism at frequencies between 1 and 0.05 Hz, which is most pronounced on the horizontal components. The noise at station n is assumed to follow Gaussian distributed white noise $\nu_n(t)$ with mean $\overline{\nu_n(t)} = 0$ and standard deviation $d\nu_n(t)$:

$$\sigma_n = \overline{\nu_n(t)} \pm d\nu_n(t). \tag{6}$$

For the construction of the data covariance matrix C_d we follow the design by Duputel *et al.* (2012). A simple diagonal matrix design with $C_d = \sigma_n^2\mathbf{I}$, $\mathbf{I}$ being the identity matrix, may result in underestimations of the uncertainties due to oversampling. This issue is tackled by additionally considering the sampling frequency of the bandpass filtered signal to compensate for this effect:

$$\left(C_d^{ij}\right)_n = \sigma_n^2 e^{-|\Delta t^{ij}|/t_0} \tag{7}$$

with $t_0 = 1/f_{\min}$ and Δt^{ij} being the time difference between sample i and j (Duputel *et al.* 2012).

2.2 Station alignment

Aligning a seismometer to true north is an important step during installation to ensure data consistency within a seismic network. While the alignment appears straight forward, especially for land stations, large discrepancies to north have been observed throughout different networks (Ringler *et al.* 2013). The alignment of OBS stations, however, is completely arbitrary and has to be estimated after the deployment. Fig. 3 displays the influence of a deviating alignment angle of $d\Phi = 10^\circ$ from true north, which we deem a realistic uncertainty in actual networks, for different source mechanisms on the radial (R) and transverse (T) component on stations at different azimuths. The three examples show that a false alignment strongly affects at least one of the components depending on station azimuth relative to the pressure, tension, and nodal axis of the mechanism. Correcting the alignment with angle Φ_n at station n can be expressed by a rotation of the horizontal components around the vertical axis Z:

$$d_n = \mathbf{R}(\Phi_n)d'_n, \tag{8}$$

$\mathbf{R}$ being the rotational matrix around the vertical axis. eq. (8) can be interpreted as a linear energy redistribution between the horizontal components R and T scaled by angle Φ_n at small deviating alignments. In practice, the true alignment angle $\Phi_{n,\,\mathrm{true}}$ cannot be derived exactly but has to be estimated within a reasonable uncertainty range:

$$\Phi_{n,\mathrm{true}} = \overline{\Phi}_n \pm d\Phi_n. \tag{9}$$

Uncertainty $d\Phi_n$ can then be translated into a general expression for the covariance matrix for the moment tensor inversion (Duputel *et al.* 2012) by:

$$\mathbf{C}_T = \int \left[d(\Phi_n) - \overline{d}\right]\left[d(\Phi_n) - \overline{d}\right]^T \rho_a d\Phi \tag{10}$$

with $\overline{d}$ being the average data vector of a population of random deviating angles according to expression (9) and ρ_a the Gaussian probability density of the alignment. This equation can be solved by a Monte Carlo approach using a large population of Gaussian distributed uncertainties in the alignment at each station. However, instead of conducting a large-scale random simulation, we benefit from the data gradient following eq. (8), which allows us to consider the sensitivity of $d\Phi$ to the horizontals for a given focal mechanism. Thus, we can give an expression for observations in the vicinity of

the true alignment to the north with:

$$d(\Phi_{n,true}) = d(\overline{\Phi_n}) + \nabla d(\overline{\Phi_n})(d\Phi_n - \overline{\Phi_n}). \quad (11)$$

Since $d\Phi_n$ is assumed to be generally small, we are able to smooth near Φ_n and write $\overline{d} = d(\Phi_n)$ in eq. (10), leading to:

$$C_T = [\nabla d(\overline{\Phi_n})] C_{d\Phi_n} [\nabla d(\overline{\Phi_n})]^T \quad (12)$$

with $C_{d\Phi_n}$ being the variance of $d\Phi$. Alignment gradient $\nabla d(\overline{\Phi_n})$ is computed numerically as a second order approximation of eq. (8) to consider clockwise and anti-clockwise alignment uncertainty:

$$\nabla d(\overline{\Phi_n}) = \frac{d'_n(d\Phi_n) - d'_n(-d\Phi_n)}{2d\Phi_n}. \quad (13)$$

2.3 uniXtree—uniform *X*-dimensional tree-importance sampling

Grid search analysis for seismic source inversion is a straightforward and robust technique to examine complex problems in arbitrary *X*-dimensional parameter space but at the cost of potentially large computational times. It is therefore important to perform the inversion efficiently by avoiding non-uniformity but at the same time allowing for fast convergence to the global minimum.

Uniform sampling of the source parameters in an evenly spaced Cartesian coordinate system, be it a direct sampling of 6-moment tensor elements or in a parametrization of five source parameters and seismic moment M_0, does not result in a uniform distribution of moment tensor solutions (Tape & Tape 2016). Likely effects are under- or oversampling of relevant or irrelevant solutions that can cause an increase of the computation time, large sampling-based uncertainties or even overestimations of local minima. A possible solution to this issue is the *n*-D hyperspace method (Tashiro 1977) that enables uniform sampling of the moment tensor elements (Staehler & Sigloch 2014) on an ellipsoid using five independent parameters and the seismic moment. This approach is straightforward as uncertainties become directly apparent on the elements. In further examinations, however, this leads to the general decomposition analysis for the full tensor to study isotropic changes and CLVD (Compensated Linear Vector Dipol) parts as well as the uncertainties in respect to the fault geometry. In this study, we use the approach by Tape & Tape (2015) where the source is represented in a geometric framework spanned by five independent angles that are directly connected to the source parameters. Strike, dip and rake are parametrized on a sphere whereas CLVD and isotropic parts are projected onto a lune. In this work, we only focus on deviatoric parameters, hence a general tectonic shear mechanism without volume changes. The remaining space has unique features with different behaviours at the boundaries:

(i) Strike with $\psi \in [0, 2\pi]$.
(ii) Dip with $\theta \in [0, \frac{\pi}{2}]$ and in the uniform Tape representation: $h = \cos(\theta)$ and its inverse with $\theta(h) = \arccos(h)$ with $h \in [0, 1]$.
(iii) Rake with $\lambda \in [-\pi, \pi]$.
(iv) CLVD $\in$ [–100 per cent,100 per cent] and in the uniform Tape representation: $v = \frac{1}{3} sin(3\gamma)$ with $\gamma \in [-\frac{\pi}{6}, \frac{\pi}{6}]$ and its inverse with $\gamma(v) = \frac{1}{3}\arcsin(3v)$ with $v \in [-\frac{1}{3}, \frac{1}{3}]$. Conversion between classical CLVD parameter to uniform parametrization γ is done by multiplying by 30/100 and back with 100/30 to convert gamma in degree and then to radian.

Using a direct sampling approach of the Tape parameters, we explore the tree-importance sampling algorithm that is extensively used for different computational problems in for example 3-D visualizations (Meagher 1982; Fujimura *et al.* 1984) or in more modern applications together with neural networks (Wang *et al.* 2017). The application to geophysical problems was first applied by Lomax & Curtis (2001) for the octant sampling of the 3-D hypocentre location. Compared to generally used techniques like the Monte Carlo or Metropolis-algorithm, it has been shown that an oct-tree algorithm is more global and complete while only depending on a few parameters. The general tree data sampling structure is recursively subdividing *X*-dimensional spaces into 2^X subvolumes. For 1-dimension the tree structure results in bisecting the search interval, whereas higher dimensions like in 3-D lead to eight subvolumes called octants (hence commonly referred to as an oct-tree). It drastically reduces the number of samples by an order of 10^5 with respective computational time while allowing for examinations of the whole model space in a robust manner. For the application to moment tensor inversion, we sample in a 4-D space spanned by ψ, h, λ and γ. Probability P_i of a source solution is then defined by the PDF $Q(\mathbf{m})$ (eq. 4) and weighted by the represented subvolume V_i with:

$$P_i = V_i \cdot Q(\mathbf{m}). \quad (14)$$

The uniXtree approach deployed, enables an efficient way to increase resolution within the full model space around highly probable solutions while only sampling coarsely volumes of less importance.

3 DATA

3.1 VoiLA OBS deployment

Between March 2016 and May 2017, a regional OBS network was installed as part of the NERC-funded international multidisciplinary consortium project—VoiLA, to study the **Vo**latiles **i**n the **L**esser **A**ntilles Island Arc (Goes *et al.* 2019). The network consists of 34 broad-band sensors deployed in the forearc and the backarc area (Collier 2015) along the arc with a focus on the northern parts (Fig. 1). During the operation time, 381 seismic events were located with high accuracy and assigned with local magnitudes (Bie *et al.* 2020). The stations were located at an average water depth of ∼2800 m with individual instruments as shallow as 812 m and as deep as 5054 m. Applying the empirical relation between water depth and the peak-frequency of related ocean induced microseismicity (Fig. 2; Yang *et al.* 2012), we find dominant ocean microseism signals between 0.008 and 0.01 Hz. Considering the resolution restriction of our local 1-D velocity model (Bie *et al.* 2020), the usable frequency range is set between $f_{\min} = 0.03$ Hz and $f_{\max} = 0.1$ Hz. This frequency band is well below the expected dominant frequency of the source–time functions for events with $M_w < 6.0$. Approximate horizontal sensor orientations were determined using the Rayleigh-wave polarisation analysis method of Doran & Laske (2017); however, formal uncertainties in these azimuths, $d\Phi_n$, can reach up to 12°.

3.2 Data selection

In this study, we focus on the northern part of the LA arc. The target area spans between 14.4°N to 18.5°N and between 60.0°W in the forearc to 62.75°W in the back-arc region (Fig. 1; black box). For later interpretive approaches, the area is further split into upper plate crustal ($z < 33$ km), slab interface ($33 < z < 100$ km) and deep intraslab ($z > 100$ km) layers as well as a northern

(>∼16.5°N) and southern sector. Initial event selection is based on local magnitudes and reported source locations by Bie *et al.* (2020). For deep hypocentre locations, a minimum magnitude of M_L 4.1 has shown to have a sufficiently high SNR while for crustal events (up to 33 km) we were able to examine events down to M_L 3.8. The minimum number of stations used in the inversions is set at 5, but the vast majority of the events have only a sufficiently good SNR on vertical components. 45 out of the 381 catalogued events (Bie *et al.* 2020) fulfil these conditions and display a sufficient enough SNR on at least the vertical components. The six largest events feature a focal solution in the USGS database (Table 1) and partially the GCMT catalogue. For the modelling of these events, we use the reviewed source information by Bie *et al.* (2020) and for the construction of the Green Functions matrix **G**, the therein published local 10 layered 1-D velocity model. As hypocentre locations and velocity model derive from the same source, we assume the influence of location errors and uncertain velocity structures to be minor, especially at the low frequencies used in the inversion. In total 39 events are new moment tensor solutions not already published in any database. We define two sets of events—the first comprising six events with FMs reported by USGS and GCMT belong to a reference event set, and the rest assigned to a new event set.

4 SYNTHETIC TESTS

To evaluate the robustness and accuracy of our inversion algorithm, we conduct a series of synthetic tests. In the first part, we study a synthetic strike-slip mechanism recorded within the station arrangement of the VoiLA OBS network, to compare the standard linear source inversion with our new Bayesian approach that takes into account the station alignment and ambient noise individually. In the second part, we examine how our inversion routine performs with various source mechanisms and the number of OBS recordings.

4.1 Influence of station alignment

Let us assume a well-distributed sub-network within the given VoiLA constellation consisting of seven receivers. The source is located at its centre and set as a pure strike-slip with $(\psi, \theta, \lambda) =$ (35,75,–5; Fig. 4). We simulate 10 000 realizations with a normal distributed alignment error at $\overline{\Phi}_n = 0^\circ$ and $\mathrm{d}\Phi_n = 15^\circ$ for each station and invert for the source mechanism in a linear L2 inversion. As expected, we observe variations between true and inverted mechanisms in strike, dip, and rake whereas the mean is at the true model. A notable change can be observed in the appearance of a non-neglectable CLVD component with a mean near zero and uncertainty of 15 per cent. A CLVD acts as an amplitude compensation on the waveforms to adjust for missing or excessive mean energy content that cannot be fully described by a pure double-couple model. In the case of false station alignments, the amplitude discrepancies on the horizontals between synthetics and observables are governed by the energy redistribution following eq. (8). While the mean CLVD in a large population of solutions is still around zero, the increased (positive or negative) uncertainty may be mistakenly interpreted as an indicator of erroneous assumptions in the wave speed model or a more complex source structure. Those assumptions might lead to a complex re-evaluation of the source and occur as a systematic error for projects using the network. A simple linear inversion algorithm is thus not able to handle such an error and will return large uncertainties.

4.2 The influence of ocean noise

In extreme cases, noise can lead to unfavourable destructive or constructive alterations of the waveforms leading to misinterpretations of local minima with subsequent ambiguous solutions and large uncertainties. We examine the difference between our Bayesian error formulation and an L2 (no covariance matrix) cost function (eq. 4). Fig. 5 displays the results for a Bayesian (data covariance matrix C_d) formulation and a L2 cost function at two different signal-to-noise ratio (SNR) levels. The top row shows the FMs for the true mechanism (blue) and the best inversion results (black). The number of the best solutions depends on the 95 per cent confidence interval of the Bayesian run and is marked as a green dotted line in the PDF graphs. Importance sampling using a Bayesian formulation suppresses improbable solutions and highlights one with high probabilities as shown by the narrow PDF. This suppression is not applicable for an L2 formulation which results in a much wider PDF covering a larger volume in the parameter space representing potentially different solutions.

For low (Fig. 5a) and high (Fig. 5b) noise the Bayesian formulation yields the true source mechanism with a corresponding level of uncertainty. In the case of L2, however, we observe also a possible thrust fault solution parallel to the tension axis of the true strike-slip mechanism. Tensional and compressional areas of both mechanisms show similarities in the recorded waveforms and can lead to wrong identification for unfavourable network configurations. If we increase the noise level, the L2 approach returns two probable solutions in the form of a normal and thrust fault parallel to the tension and pressure axis, respectively.

4.3 Influence of the VoiLA network geometry

Based on the network geometry of the VoiLA network, a subset consisting of a given number of stations within a source-receiver distance of 350 km are randomly chosen to perform source inversion for arbitrary double-couple mechanisms. We choose the location of ev123—an earthquake located in the middle of the network—as fixed hypocentre location (Tab.1). For each experimental setup at least 10.000 random realizations have been conducted. Discrepancies between true and resulting deviatoric source solution are measured using the Kagan angle (Kagan 1991) and absolute percentile changes in the CLVD. All discrepancies are then ascending sorted and normalized on their number. Coloured curves in the results plots represent the exceedance frequency for a given discrepancy of Kagan or CLVD. To compare the performance of different inversion approaches, we calculate a reduction percentage between the L2 and the Bayesian formulation:

$$\text{reduction} = 100 \cdot \left(1 - \frac{\sum pdf_{\text{Bayesian}}}{\sum pdf_{L2}}\right). \tag{15}$$

4.3.1 Performance using data covariance C_d

The Bayesian error formulation uses only the data covariance matrix C_d. In the construction of the matrix, 50 per cent of the simulated vertical peak noise amplitude of each trace is set as σ_n in eq. (7). The station-wise simulated noise on the horizontal components is then rescaled with a constant factor between the horizontal to the vertical peak noise amplitude (H2V). Our tests were conducted for 4, 6 and 8 random distributed stations but with a fixed source location. To restrict the number of free parameters, we keep the magnitude fixed.

Table 1. Table of reference events. The table features two different depth information (in order): the depth given by USGS and the depth (blue) derived by Bie *et al.* (2020). Lateral information are similar in both sources, displayed are the location by Bie *et al.* (2020) which we also use in the inversion process. Entries marked in blue are findings of this study. Our beachballs are displayed for 95 per cent (black) and 97.5 per cent (red) probability solution.

ID	Day Onset-Time	lat | lon depth | depth	M_w M_w	FM FM	CLVD CLVD	Lit. USGS	This Study
ev106	2016-05-09 13:36:27.76	16.179 | –60.615 23.9 | 32.34	4.4 4.7	77,57,–115 78,57,–114	-22 —		
ev122	2016-10-14 17:25:24.00	16.723 | –60.655 25.3 | 10.65	4.4 4.7	180,2,105 179,83,–79	-4 —		
ev123	2016-10-18 22:07:43.75	15.298 | –61.352 146.0 | 159.62	5.6 5.6	248,44,–106 246,42,–93	2 8		
ev143	2017-02-03 19:53:52.86	15.065 | –60.457 44.0 | 51.14	5.80 5.9	334,59,86 341,55,87	1 -2		
ev152	2017-04-17 06:24:41.40	17.513 | –61.025 18.7 | 20.59	4.8 5.0	133,37,–87 140,68,–70	9 2		
ev155	2017-04-25 09:53:31.81	16.835 | –60.915 38.5 | 15.71	4.4 4.5	336,79,82 9,61,80	11 —		

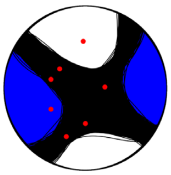

Figure 4. Influence of station alignments on a distinct strike-slip source solution. Effect of 10 000 Gaussian distributed station alignments with mean $\overline{\Phi}_n = 0$ and standard deviation $d\Phi_n = 15^\circ$. Red dots mark the piercing points of rays at the stations.

Fig. 6 summarizes the results of the random sample study at all setups. Displayed PDF curves represent the ascending discrepancy normalized by the number of random realizations (>10 000). The average discrepancy in the Kagan angle and CLVD percentage increases proportionally to the H2V factor and with decreasing number of stations. Significant differences appear between the L2 and the Bayesian formulation, where the Kagan angle and CLVD percentage is predominantly smaller using the latter approach. Especially the error to the true CLVD could be reduced (relative reduction of the areas below the curves following eq. 15) by around 48 per cent at a horizontal H2V factor of 1.0 and up to 59 per cent at larger noise with H2V factor 2.0. Reduction of the Kagan discrepancy is again smaller for H2V factor 1.0 at 20–28 per cent but much better at H2V factor 2.0 with a reduction of up to 41 per cent. In all settings, however, we can observe significant outliers in the Bayesian approach of the Kagan angle at H2V factor 1.0. These outliers are due to the underestimation of errors, arising from the definition of the data covariance matrix C_d (eq. 7), that are ignored in the L2 approach. Average noise amplitude σ_n is measured before the origin time at each station and assumed to be stationary and uncorrelated white noise. This assumption, however, depends on the absence of unknown transient signals (Vasyura-Bathke *et al.* 2021). Influential is also on the frequency band of the data and the sampling rate that might result in pessimistic uncertainty estimations following the eq. (7).

4.3.2 *Performance using data and model covariance C_D*

Station alignment on the observed data affects the full waveform information on the horizontal components, hence noise and transient signal. The model covariance matrix C_T is constructed based on the synthetics, which display the pure transient signal without any noise. This allows us to directly examine the uncertainties on the earthquake signal itself, while noise is handled by the data covariance matrix C_d (eq. 5). For the construction of C_T, we assume an average alignment angle $d\Phi_n$ (eq. 12) of 10° at all stations within a chosen network configuration. As this magnitude of $d\Phi_n$ represents only a small variation, the inversion problem can be treated in a first-order approximation as a linear energy redistribution between the horizontal traces (eq. 11).

Given that alignment mainly affects the horizontal components with low energy content (Fig. 3), we need to consider a low noise level. This assumption stands valid, as small magnitude events within a comparatively high horizontal noise level, as is the case for OBS recordings, are mostly restricted to vertical recordings and hence are independent of this error source. In contrast to that, large events with a good SNR are more affected by small alignment uncertainties as there are potential non-negligible inferences between the two error sources.

We design a synthetic study for a base noise of 30 per cent of the vertical trace and no additional amplification H2V factor on the horizontal components (H2V factor 1.0). General settings are adopted from the previous noise examination for 4, 6 and 8 random distributed stations.

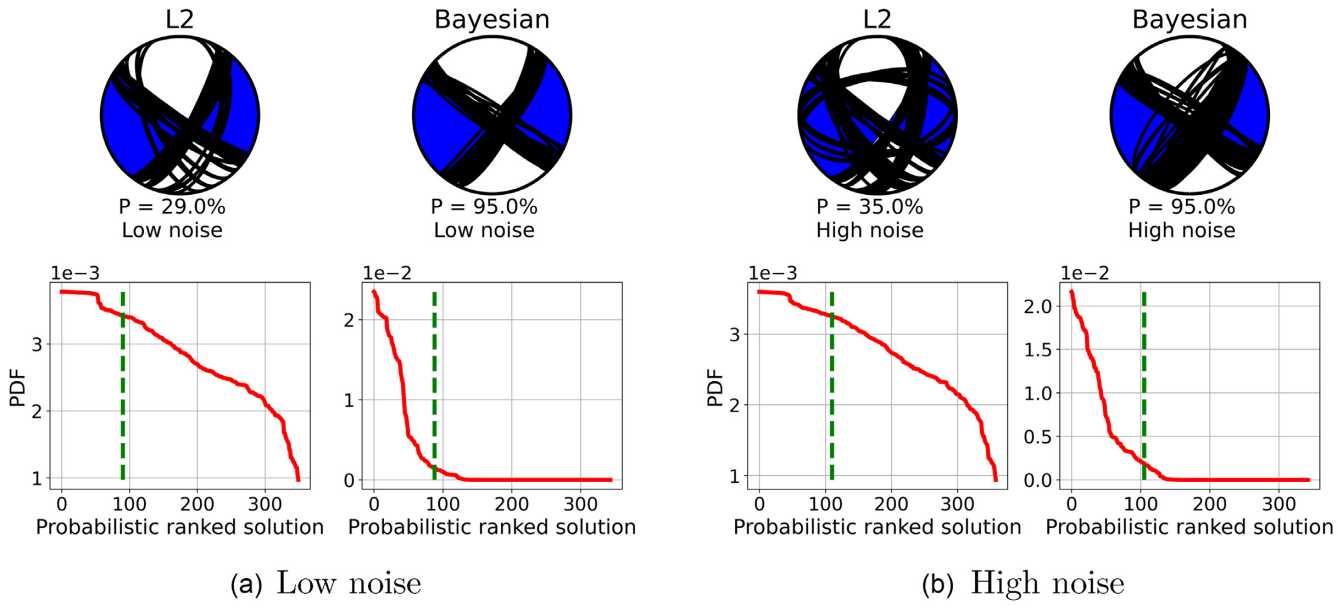

Figure 5. Pure DC inversion results for a strike-slip mechanism using a L2 and a Bayesian error formulation. Simulations are performed for low noise (a) and a high noise level (b). True source solution is displayed in blue with top solutions marked by black lines. Below each beachball is the sorted probability density function, the green vertical dotted line marks the top 95 per cent of the Bayesian solution and the corresponding number of samples in the L2 inversion at the same noise level.

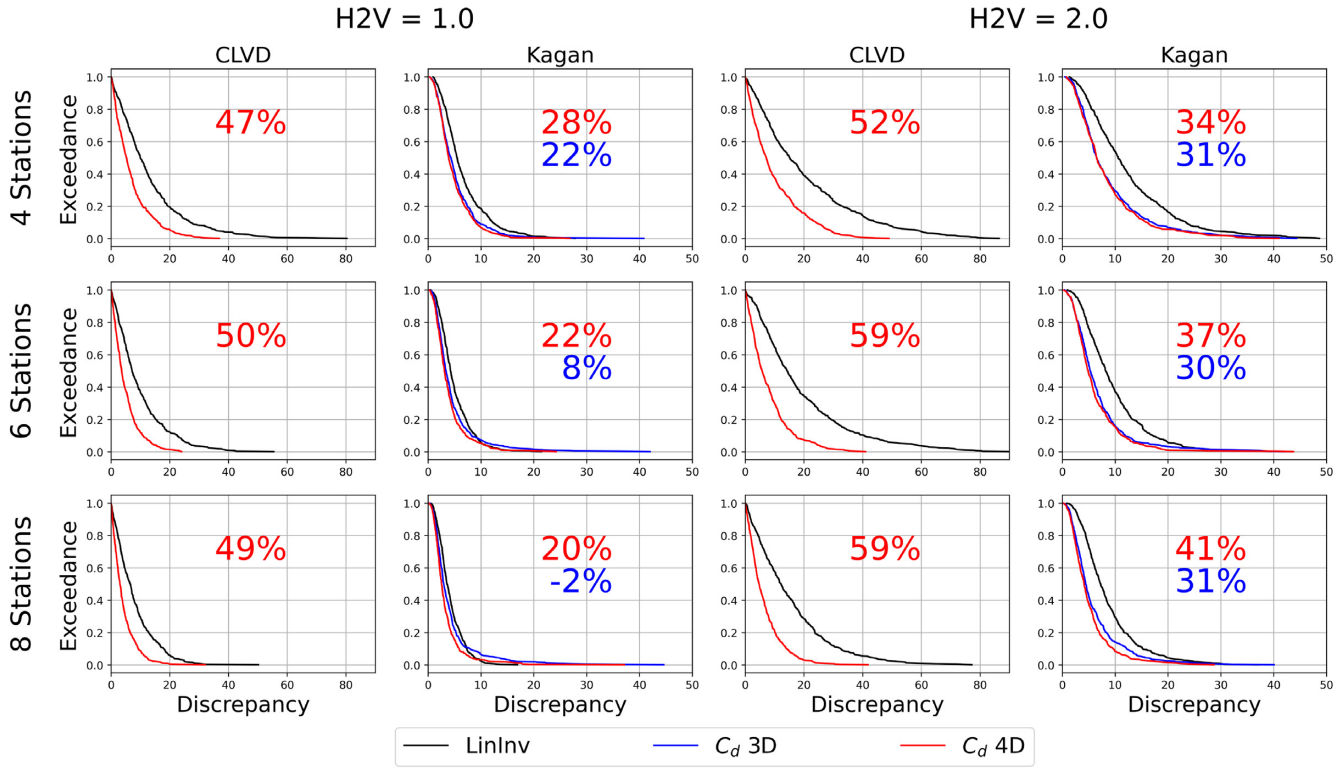

Figure 6. Synthetic noise test with base amplitude level at 50 per cent of vertical peak signal. Marked as black curves are the results for a simple linear inversion while red is a Bayesian formulation using a data covariance matrix C_d in a deviatoric tree-importance sampling. Corresponding percentage values are the relative reduction of the curve integral between the L2 to the Bayesian formulation.

Fig. 7 summarizes the results of the random study at all surveyed setups. Displayed curves follow the same notations as in Fig. 6 but with a third one representing the discrepancy of a C_D sampling. For the CLVD we observe a much smaller reduction between the L2 and Bayesian inversion. While the noise conditions are the same in the previous tests with horizontal H2V factor 1.0, it becomes apparent that changes are attributed to the additional station alignment. Differences, however, can be observed between a C_d inversion and and a C_D inversion (eq. 5). While comparatively small, the C_D setting is generally better compared to the C_d inversion and increased with

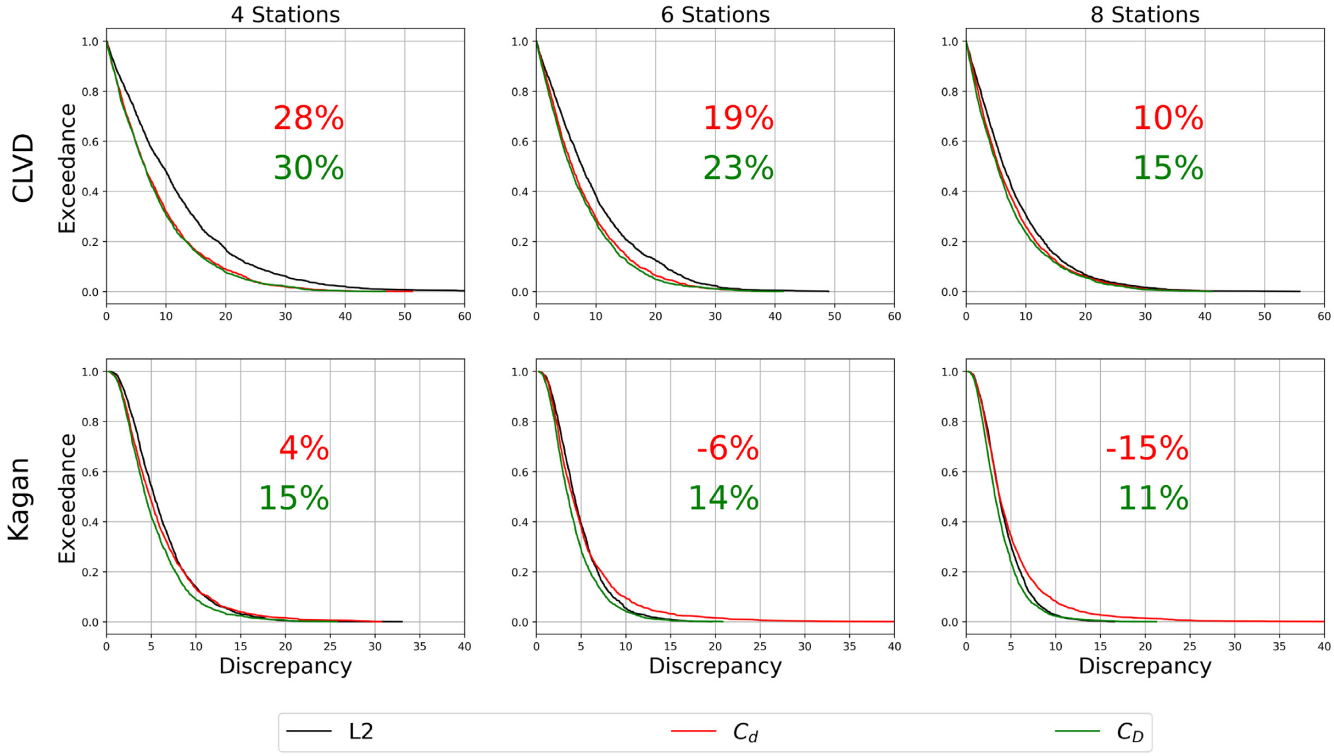

Figure 7. Synthetic alignment test at 30 per cent vertical base amplitude with horizontal to the vertical peak noise amplitude (H2V) factor of 1.0 and 10° mean Gaussian distributed station alignment angle. Displayed PDF curves follow the same notation as in Fig. 6 but with a fourth curve (green) displaying the results of a Bayesian C_D formulation.

the number of stations. For the Kagan angle, we observe a strong worsening of the C_d inversion in contrast to a C_D inversion. Like in the previous test (Fig. 6) low probable outliers become notable in a C_d inversion but do not appear in the C_D inversion.

4.3.3 Effects of restriction on vertical recordings

For most of the earthquakes in our OBS database, we expect a limitation to the vertical recordings, especially for events at the lower end of the resolvable magnitude range ($M_w < 4.8$). In a final synthetic study, we examine the effects of a vertical component analysis in comparison to a three-component analysis. In practice, most inversions of small magnitude events are not only limited on the vertical recordings but also to a comparable small and potentially badly distributed network. A full deviatoric description of such sources might hereby be misleading as the CLVD affects the amplitudes of all three components on a different scale. We hereby follow our previous setup with a base noise level of 50 per cent of the vertical peak amplitude.

As before we can observe a significant reduction of the CLVD discrepancy (Fig. 8), but 10–20 per cent smaller compared to an inversion using three components (Fig. 6). In an absolute comparison between a vertical and three-component inversion, we note a drastic worsening compared to the case with an H2V factor of 1.0 and a similar level at H2V factor 2.0. Assuming that a restriction on only vertical data is attributed to an H2V factor exceeding 2.0, inversion results can be expected to be generally better compared to using all three components. A similar pattern can be observed for the Kagan angle. Interestingly the reduction of the discrepancy in the Kagan angle using a pure double couple inversion becomes similar to that of a deviatoric inversion.

5 RESULTS

5.1 Reference event set

During the VOILA deployment, various international agencies (e.g. USGS, GCMT, GEOPHONE) reported source mechanisms for six local earthquakes. These six events define our reference event set, which is used to test the performance of our inversion algorithm with real data. We find large discrepancies in the source depth between the USGS locations and the relocated hypocentres of Bie *et al.* (2020), that we fixed for all inversions. All derived MT solutions show a high degree of similarity with published solutions. In the following, we will highlight the inversion results and detailed comparison for the three largest events (Table 1).

Event ev143, the largest earthquake in our observation period with a moment magnitude of M_w 5.9, occurred on 3 February 2017, at 19:54:22.86 UTC at a depth of around 50 km within the fore-arc region east of northern Martinique. We use a total of 19 OBS stations for the inversion but are restricted to using mainly vertical components as most horizontal components exhibit saturation due to strong ground motion in the near-field. The derived mechanism depicts a thrust fault with (strike,dip,rake) = (341,55,87) and a CLVD of –2 per cent. Our result slightly differs in the dipping angle (by about 11°) compared to the USGS solution (334,66,84) but shows much higher similarity to the GCMT solution (334,59,86). The derived half duration is, according to the USGS database, at 4.0 s, which is well above our defined frequency band.

Event ev123 occurred on 18 October 2016, at 22:08:13.75 UTC offshore Martinique. With a depth of approximately 160 km and a moment magnitude of M_w 5.6, it is the strongest earthquake in this region since the 2007 M_w 7.4 Martinique event. Its central location provides good azimuthal coverage and good SNR on

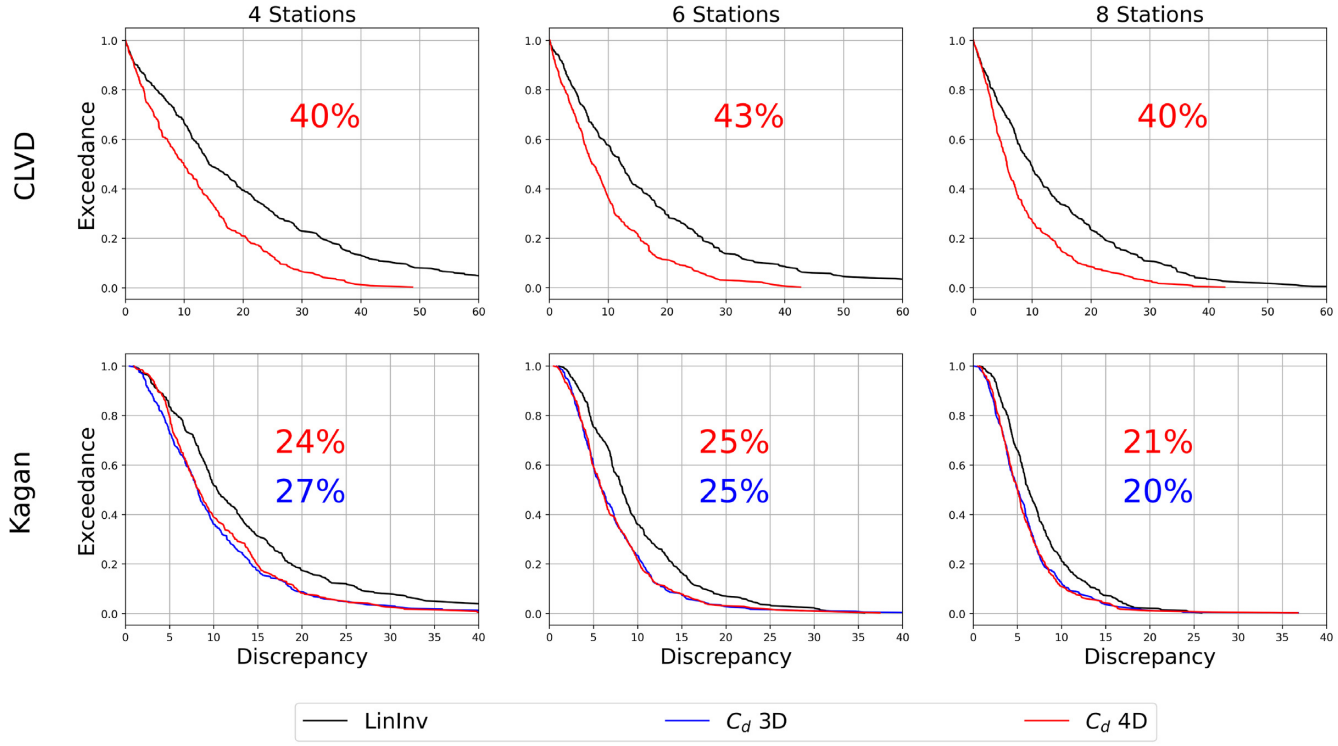

Figure 8. Comparison of a vertical trace (1C) data restricted inversion versus a three component (3C) inversion in a synthetic noise test at 50 per cent vertical base amplitude. Displayed PDF curves follow the same notation as in Fig. 6.

all three components of at least seven stations. We utilized a C_D Bayesian inversion, as we have a sufficient SNR on all three components. Our results (246,42,–93) indicate a trench perpendicular normal fault that is in good agreement with the solutions obtained by USGS (251,43,–100) and GCMT (248,44,–106) but with an increased CLVD of ∼8 per cent in our solution.

The third event, ev152 with a magnitude of M_w 5.0, occurred on 17 April 2017, at 06:25:10.47 UTC at a depth of 21 km. It is part of the most active cluster in the northern shallow forearc offshore Antigua during our deployment. The derived mechanism displays a trench parallel normal fault with a small positive CLVD part of 2 per cent but shows discrepancies in the double-couple part between our (133,37,-87), the USGS (140,68,–70), and the GCMT (106,40,–125) solutions. The remaining three events are only listed in the USGS database but are generally consistent with our solutions (Table 1).

5.2 Combined MT catalogue for northern LA subduction zone

We compile a catalogue of 151 MTs that includes 29 local solutions by (Gonzalez *et al.* 2017), 22 from (Ruiz *et al.* 2013) who focused on a small area east of Dominica and Martinique, 55 teleseismic solutions from various agencies (GCMT, Geofone and USGS) and 45 derived by Bayesian inversion of OBS waveforms in this study. We mapped this catalogue into a focal mechanism classification (FMC) diagram (Álvarez Gómez 2019) and the crustal events are divided manually into five groups based on their FMC location and mechanisms (Fig. 9). All events below 100 km depth form the sixth group that contains a variety of mechanisms but is dominated by NFs. We plot all events (colour-coded for each group) in map view (Fig. 10) together with key features such as projected fracture zones, slab depth-contours and projected rupture areas of the 1839 and 1843 events. We show three cross-sections (A,B,C) that intersect important tectonic/geodynamic features. The unprecedented quantity of MTs enables a detailed analysis of the earthquake source mechanisms within our target area.

5.2.1 Plate interface seismicity

Seismic activity at the plate interface is marked by thrust events (dark blue mechanisms) at 50 ± 10 km depth and shallow dipping thrust events (light blue mechanisms) close to the trench (Fig. 10). The dip angles follow the subducting slab geometry. In the northern area (16.5°N–18.5°N) particularly, the thrust events at various depths define a wide seismogenic interface between the subducting and overriding plates. This zone overlaps with the estimated rupture area of the 1843 *M*8.5 earthquake—the largest megathrust event in the LA recorded in history (Feuillet *et al.* 2011b). To its south (15.0°N–16.5°N), a lack of thrusting and shallow dipping events is consistent with previous studies (Gonzalez *et al.* 2017). To the east of Martinique (15.0°N,−60.5°W), several thrust events are found within the estimated rupture area of the 1839 *M*7.5 megathrust event (Feuillet *et al.* 2011b; Fig. 10, zoom box 2), and there are no shallow dipping thrust events near the trench as found in the north.

5.2.2 Upper-plate seismicity

Normal faulting (red mechanism) dominates the upper-plate seismicity, with sporadically scattered strike-slip (dark green mechanism) and oblique normal/thrust faulting to strike-slip (NF/TF to SS) events (light green mechanism). The northernmost sector of our target area shows an larger number of oblique events relative to the south. While the occurrence of oblique events decreases towards

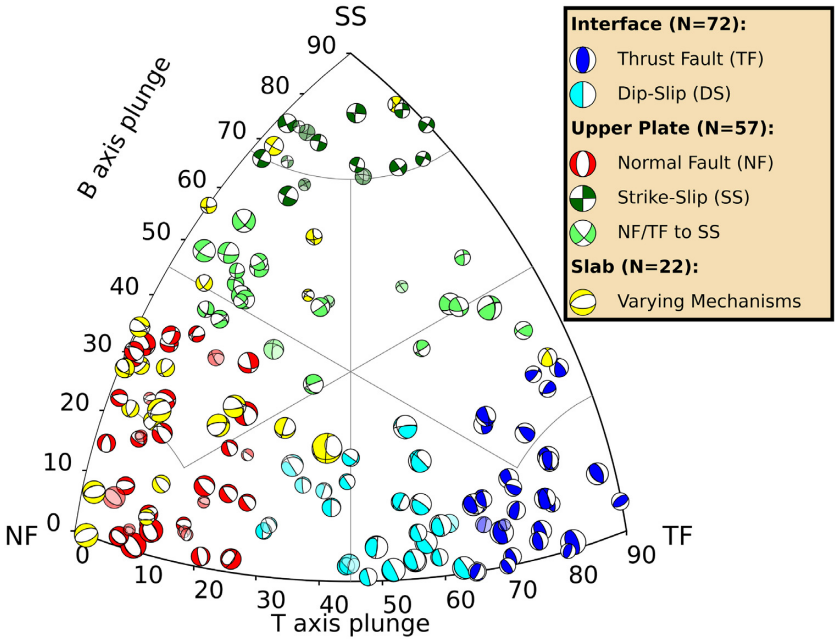

Figure 9. Focal Mechanism Classification (FMC) diagram. Displayed are all available focal solutions in the target area. The mechanisms are split into 6 groups manually, based on their locations in the FMC diagram: normal faults (NF; red), thrust faults (TF; blue) dip-slips (cyan), strike-slips (SS; dark green) transition events to strike-slips (NF/TF to SS; light green) and a special group containing all events below 70 km (yellow). Events without certain depth information (e.g. Gonzalez *et al.* 2017) are displayed in faded colours. The diagram was created using a modified python routine based on Álvarez Gómez (2019).

the south, normal faulting events become more frequent, especially near event ev152. The highly active cluster produces at least five $M_L > 3.9$ events in a day (Bie *et al.* 2020) and features a mixture of normal and NF/TF to SS transitional events (Fig. 10, zoom box 1). With an average depth of 20 km, this cluster is near the plate interface where we can also observe several shallow dipping thrust events just below and surrounding it. Normal faulting events in the crust increase in the southern sector particularly between Guadeloupe and Dominica (15.8°N,61.65°W). A prominent event of this cluster is the shallow 2004 M_w 6.3 Les Saintes earthquake which ruptured part of an arc-parallel en echelon fault system (Feuillet *et al.* 2011a). The main shock triggered up to 30 000 aftershocks within the following two years and is one of the largest instrumentally recorded seismic events in the LA (Feuillet *et al.* 2011a). We observe additional normal faulting events close to the interpreted upper plate Moho (Fig. 11, profile B), striking in the trench perpendicular direction. Further south, large-magnitude crustal events are rare.

5.2.3 Slab seismicity

The deep group covers all seismic events with depths greater than 100 km and these locate within the subducted slab. In the northern sector, only three deep events were observed which may be attributed to comparably small magnitudes and unfavourable station coverage in these parts of the arc. The most active zone is between Dominica and Martinique. At ∼150 km depth, this area hosts the majority of strong ($M_w > 4.0$) deep earthquakes along the LA Arc within the instrumented period. MT solutions show highly complex faulting structures consisting mostly of normal faults but also a few strike-slip faults and one thrust fault. The normal faults display different fault orientations but are predominately aligned perpendicular to the trench. The largest earthquake within this group is the 2007 M_w 7.4 Martinique earthquake, the to-date strongest instrumentally recorded seismic event in the LA. The large ∼95 per cent CLVD part of this event hints at a much more complex source mechanism than pure normal faulting.

5.3 Stress inversion

The state of stress in the LA is governed to first order by the subduction of the Atlantic oceanic lithosphere beneath the Caribbean Plate. In most cases, especially for small and intermediate-sized events, rupture occurs on pre-existing weak faults that do not necessarily coincide with the current main stress axis (Plenefisch & Bonjer 1997). The origin of small-scale stress perturbations includes anisotropy, fluid pressure variation, or mineral heterogeneity (Plenefisch 1996). Large events in the subducted lithosphere are likely related to the reactivation of pre-existing faults that formed in past stress conditions (e.g. Delescluse *et al.* 2008; Garth & Rietbrock 2014). To gain insights into the local stress conditions, we perform stress inversions for the interface, crustal and deep event groups based on our combined catalogue. We use the STRESSINVERSE package (Vavryvcuk 2014) which is based on the approach by Michael (1984) but in an iterative joint inversion, reducing the ambiguity problem due to the identification of active and auxiliary planes. STRESSINVERSE takes as input the source geometry (strike/dip/rake) of a group of events and returns the principal stress directions with $\sigma_1 > \sigma_2 > \sigma_3$ and the scalar quantity R ($0 \leq R \leq 1$) describing the magnitude of σ_2 relative to the others (Gephart & Forsyth 1984):

$$R = \frac{\sigma_1 - \sigma_2}{\sigma_1 - \sigma_3}. \tag{16}$$

We assume for each inversion run a mean deviation of 10° in a realization of 250 normally distributed variations.

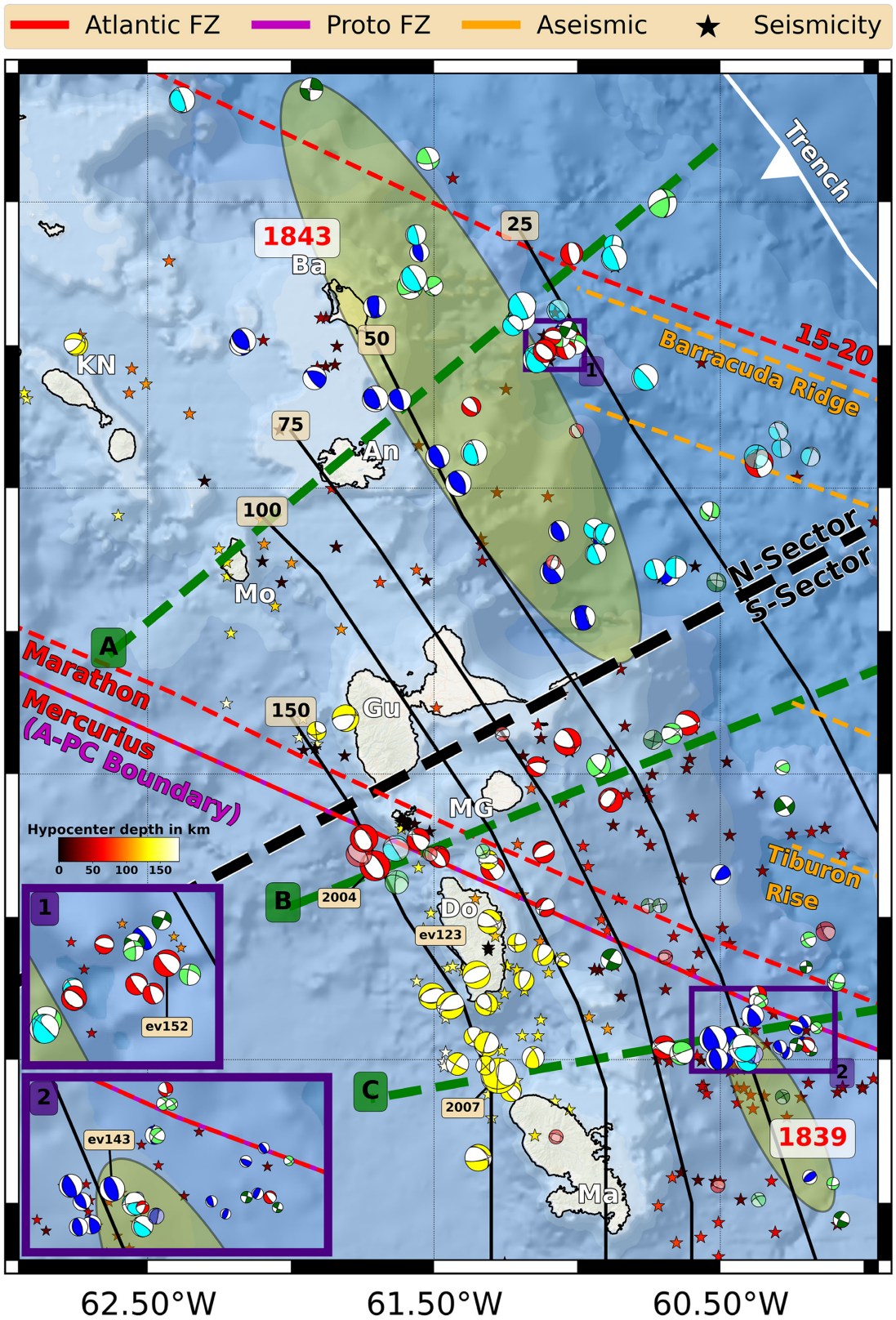

Figure 10. Distribution of all existing focal mechanisms from USGS, GCMT, Gonzalez *et al.* (2017) and this study corresponding to the colour-coding displayed in the FMC-diagram (Fig. 9). The map covers the islands of Antigua (An), Barbuda (Ba), Saint Kitts and Nevis (KN), Monserrat (Mo), Guadalupe (GU), Marie-Gelante (MG), Dominica (Do) and Martinique (Ma). Depth profiles (green), subducted fracture zones (red: Atlantic; magenta: Proto-Caribbean), oceanic ridges (orange) and trench (white) are introduced in Fig. 1. Displayed ellipsoidal patches represent the locations of the 1839 and 1843 events (Gonzalez *et al.* 2017). Black lines represent the depth profiles of the slab model and depth coloured stars the relocated seismic events recorded during the VoiLA deployment (Bie *et al.* 2020).

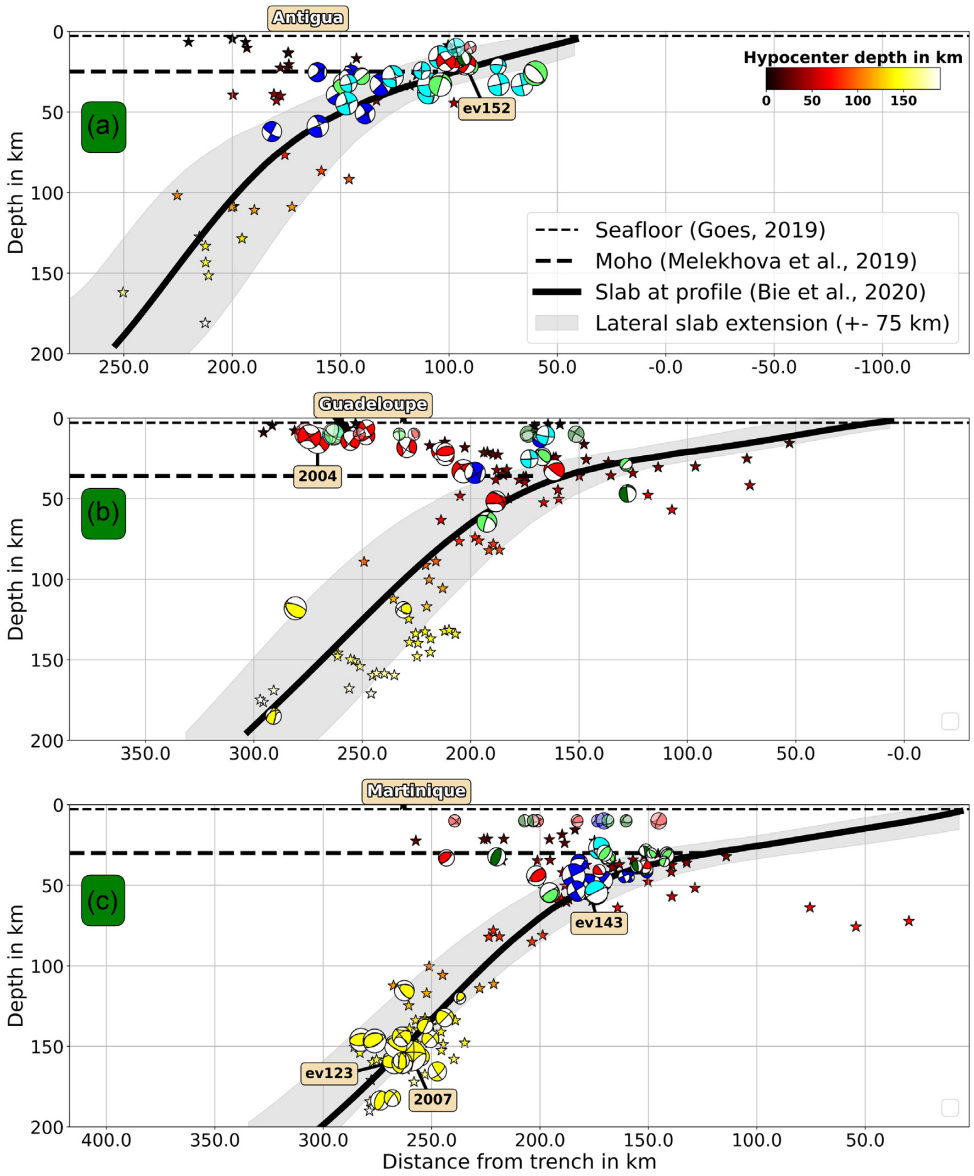

Figure 11. Cross-section plots along depth profile A, B and C. The featured seismicity and local slab model is derived by Bie *et al.* (2020). Grey shaded area surrounding the slab curve at the profiles indicates the lateral extension to north and south (±75 km).Thick dotted lines represent the average Moho depth at the profile intersection (Melekhova *et al.* 2019) with the above thin dotted line being the average water depth of 2.8 km at which the OBS sensors are located (Goes *et al.* 2019). Colour-coding of the displayed beachballs corresponds to the FMC-diagram (Fig. 9). Faded beachballs do not have depth information and are set to a default depth of 10 km.

Initial stress inversions were performed for the plate interface events and upper plate events separately. The former group includes 50 thrust MTs with the inversion showing a compressional stress regime with $R = 0.52$. The direction of σ_1 is trending 61° and plunging 25° (Tab.2) in good agreement with the local slab model (Bie *et al.* 2020) which depicts an average dip of 30° and a mean azimuth of about 60°. In the upper plate, inversion of 73 MT solutions depicts a trench parallel extension stress regime with σ_3 azimuth at 183° and plunge 3° and $R = 0.87$. The southern sector contains a large number of trench perpendicular normal faults, suggesting a stress rotation compared to the northern sector. We further examine the local stresses of the northern and southern sectors separately.

Interface activity in the northern sector shows widespread slab parallel thrusting and shallow dipping thrust events while we observe only a small active cluster in the south showing slightly different striking directions (Fig. 10). The stress inversion for 38 events results in azimuth and plunge of σ_1 consistent with the average slab geometry striking ∼63° and dipping ∼29° in these parts (Profile A, Fig. 11). Stress inversion for the 15 events further south, however, shows a nearly slab-dip parallel compressional regime with maximum stress σ_1 at 88° and a near-horizontal thrust angle 84°. A reduced R (0.32) indicates a more complex stress field compared to the northern part.

Upper plate seismicity is mainly normal faulting with a subset of strike-slip and NF/TF to SS transitional events. The stress inversion of 22 events in the northern crust reveals a transitional regime from strike-slip to normal faulting (Lund & Townend 2007) with σ_1 direction of 119°. The small scale quantity $R = 0.12$ shows a large influence of σ_2 and suggests a strike-slip component. Further south we observe a rotated, arc-perpendicular stress regime with

Table 2. Stress inversion.

Layer	Region	N	σ_1 azimuth in °/ plunge in °	σ_2 azimuth in °/ plunge in °	σ_3 azimuth in °/ plunge in °	R
Interface	Arc	53	61/25	153/3	248/65	0.52
Interface	North	38	63/29	157/8	262/60	0.55
Interface	South	15	88/84	359/9	150/80	0.32
Upper plate	Arc	73	75/80	274/10	183/3	0.87
Upper plate	North	22	119/55	340/28	239/19	0.12
Upper plate	South	51	234/88	70/2	340/1	0.80
Slab	South	18	54/71	273/15	180/11	0.69

σ_3 trending 340° and σ_1 plunging nearly vertically in a largely diffuse striking direction. The scale quantity indicates normal faulting dominates with $R = 0.80$, compared to the north.

We perform a single stress inversion for the deep earthquake group in the southern sector. In this inversion, we include 20 deep events, spatially clustered between Dominica and Martinique at ∼150 km depth. Contrasting to the stress condition on the interface at shallow depth, the deep events depict a slab-dip perpendicular extensional stress regime with σ_1 orientating parallel (54°) to the slab and plunging steeply at 71°. The scale quantity R equals 0.69.

6 TECTONIC IMPLICATIONS

6.1 Interface activity

At depths shallower than 50 km, we find a dominance of thrust activity and further towards the trench, shallow dipping thrust events become more frequent. This agrees with previous studies in the region (e.g. Gonzalez *et al.* 2017) and implies seismic slip along the megathrust between the subducted slab and overriding plate. In the northern sector (Fig. 12a), the stereo plot of the stress regime depicts widespread activity with the pattern of a classical subduction zone. Most of the events are located within the estimated rupture area of the 1843 *M*8.5 earthquake (Feuillet *et al.* 2011b). The occurrence of these thrust events corroborates that the 1843 event was a megathrust earthquake that ruptured the seismogenic part of the plate interface, instead of being within the subducted lithosphere (van Rijsingen *et al.* 2021). The southern sector lacks such compressional events except for in a small but highly active cluster (Fig. 10; Zoom Box 2) within the area of the 1839 *M*7.5 event to the east of Martinique which is also assumed to be an megathrust event (Feuillet *et al.* 2011b). The stereo plot for the southern sector indicates a much more diffuse pattern featuring a range of fault strikes, but still with an overall trench-perpendicular compressional stress that appears to rotate along with the curve of the island arc (Fig. 12a).

6.2 Upper plate activity

Upper plate activity comprises a majority of normal faulting events but also includes a subset of SS and NF/TF to SS transitional mechanisms. Transitional events occur primarily in the northern sector, where our results (Fig. 12b) indicate a rotational stress regime (Lund & Townend 2007). Such rotation may be related to the transition from a sinistral strike-slip system at the northern end of the LA subduction zone, towards an approximately arc perpendicular extensional faulting regime (Julien & Bonneton 1989; Laurencin *et al.* 2017). In the midst of this area, we recognise a small cluster of events with a variety of mechanisms (Fig. 10; Zoom Box 1) centred at a depth of around 20 km, still within the Caribbean crust but near to the interface zone. The cluster is located above the projected position of the Barracuda Ridge after subduction, inferring a possible link between them. Seaward of the trench, the Barracuda Ridge rises 1800 m above the surrounding seafloor and is topped by a very thin sedimentary drape (Patriat *et al.* 2011). Previous work did suggest this feature would have an effect on upper plate deformation (McCann & Sykes 1984; Laigle *et al.* 2013a), as seen in our study. The stress regime of the upper plate evolves from the transitional regime of the northern sector towards a dominance of arc-parallel extension in the south (Fig. 12b). However, even though the overall stress tensor in the southern sector indicates arc-parallel extension, events in the vicinity of the 2004 *M*6.3 Les Saintes earthquake reflect arc-perpendicular extension consistent with the arc-parallel en-echelon faults identified by Feuillet *et al.* (2011a). While interpretations for events to the east of Martinique are limited by the small event set and mostly missing depth information, we recognise on cross-section profile B (Fig. 11; B) that the depths of upper plate normal faulting increase towards the east. The events with shallow depths west of and aligned with the arc correspond to arc parallel normal faulting of the Les Saintes earthquake swarm. Their shallow depths and overall smaller contribution to the total moment released in normal faulting in the southern segment, may be due to the relatively high crustal temperatures at and near the arc. Eastwards, in the forearc, azimuthal directions of the normal faults become mostly arc perpendicular as their depths increase towards the interface zone. This change in style is consistent with change in orientation of the faulting structures identified by active seismic imaging (Feuillet *et al.* 2011a), and indicates that the forearc is characterised by stresses associated with along-arc bending and oblique subduction (Feuillet *et al.* 2002) while the arc and backarc are dominated by trench-perpendicular extension as expected due to pull of the underlying slab, possibly exploiting structures formed during previous phases of backarc opening (Allen *et al.* 2019).

6.3 Slab activity

Seismic activity within the intermediate-depth range (70–300 km) concentrates between Dominica and Martinique. Here the comparably large size of our MT database ($N = 18$) and the high quality event locations (Bie *et al.* 2020) allow us to perform an examination of the activity that we attribute to intraslab seismicity. This cluster encloses several large magnitude events, including the 2007 M_w 7.4 Martinique event and the M_w 5.8 ev123 event of the VoiLA catalogue (Tab.1). Both moment tensor solutions have a relatively large CLVD component suggesting a complex rupture history. In general, this cluster shows predominantly normal faulting activity with fault strikes in a trench perpendicular direction in the north (under Dominica) and trench parallel towards the south (between Dominica and Martinique). We also find a more variable set of mechanisms

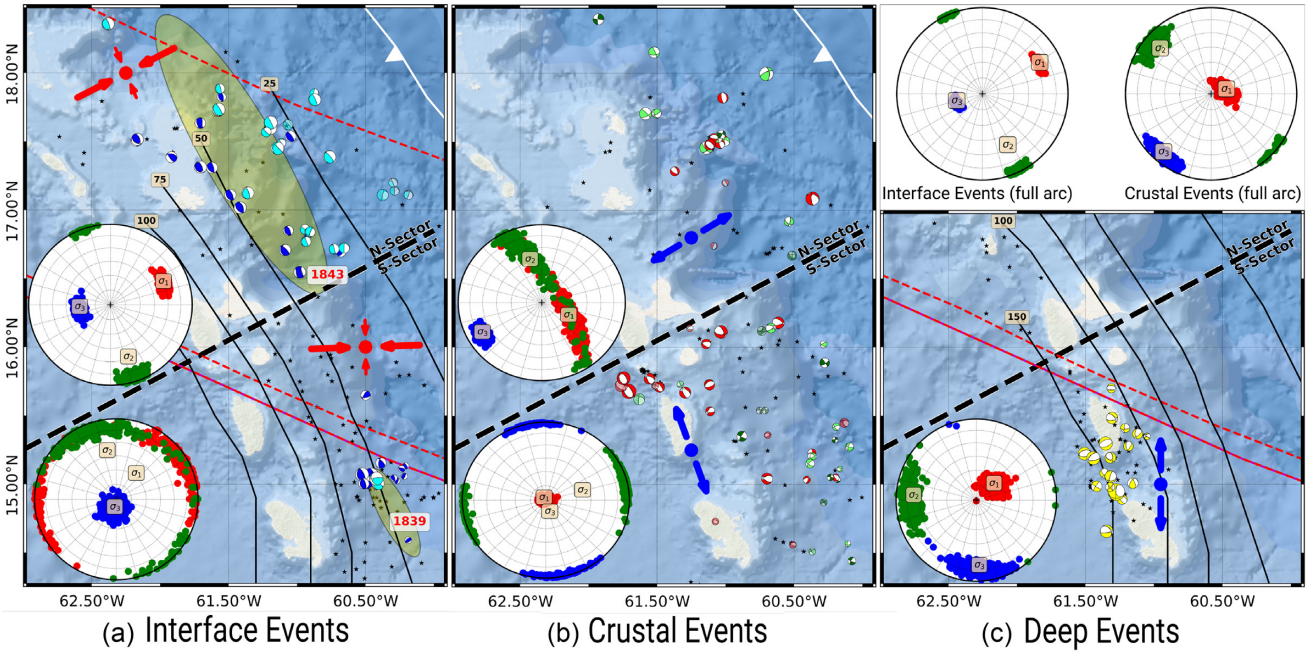

Figure 12. Results of stress inversion of (a) interface, (b) crustal and (c) deep events in the northern and southern sector. Top-right shows the inversion results of the interface and crust without regional sectoring.

including some strike-slip and a single thrust mechanism in the vicinity of the 2007 Martinique event. The dominant stress condition is downdip compression (as σ_1 axes are most strongly clustered) and slab parallel extension (Fig. 12c). Most subduction zones exhibit downdip extension at intermediate depths, but a few without deep seismicity (below 300 km depth) display downdip compression within the 100–200 km depth range, including New Britain, Ryukyu and the central Aleutians, as well as a few other segments of trenches with deep seismicity (central Tonga, northern Kuriles) (Chen *et al.* 2004; Alpert *et al.* 2010; Bailey *et al.* 2012). Some further exceptions of this can be found in more complex settings like South Sandwich that exhibits a local stress reversal in depth below 150 km (Giner-Robles *et al.* 2009), in Calabria with downdip compression between 200 and 300 km depth (Bailey *et al.* 2012) or the Hellenic arc with a slab perpendicular compressional stress regime at its centre (Rontogianni *et al.* 2010).

Downdip compression at intermediate depths may be the result of a relative high resistance to sinking into the lower mantle (Goes *et al.* 2017), which would be consistent with the interpretation from Braszus *et al.* (2021), that subducted slab material from 70 Myr ago to present has accumulated in the upper mantle below the Antilles. In most of the slabs with downdip compression at intermediate depths however, the extension is oriented slab-perpendicular, while in the Antilles, the extension is dominantly slab-parallel (Fig. 12c). Geometric effects of a curved slab are not sufficient to explain the rotational behaviour of the Antillean intermediate-depth normal faults. Along-strike bending would introduce along-strike compression on the inside of the bend as well as along-strike extension on the outside of the bend. One might expect that the compression closer to the colder slab top might be more prominent in seismicity, yet we see only extension. Trench-parallel extension was found in the northern Hikurangi subduction zone, New Zealand (Okuwaki *et al.* 2021); however, this stress pattern was attributed to a subducting oceanic plateau or seamounts in a centroid depth of only around 70 km, which is not a likely mechanism for the LA. Wadati-Benioff seismic activity below central LA has long been hypothesized to be influenced by a gap in the slab near 15°N (Bie *et al.* 2020). Seismic anisotropy from teleseismic SKS waves (Schlaphorst *et al.* 2017) was interpreted as due to mantle material flowing through a gap within the subducted lithosphere at around 170–200 km depth. A gap at this location was also supported by teleseismic tomography models (Benthem *et al.* 2013; Harris *et al.* 2018) of the central parts of the arc (∼15°N). A recent teleseismic tomography study, however, by Braszus *et al.* (2021) showed that any gap is confined to the deep upper mantle and the slab looks continuous at the depths of the seismicity. Instead Braszus *et al.* (2021) observes a wave speed anomaly that can be attributed to a signature of excess slab hydration within the subducted Proto-Caribbean Plate, possibly near the subducted spreading centre. The seismicity does reveal a change in slab dip (Fig. 11), with the northern part of the slab being steeper and deeper than the southern part, but the vertical offset is not sufficient to generate a gap in the slab (Bie *et al.* 2020). Furthermore, Bie *et al.* (2020) find no sharp changes in the slab dip angle that would be expected if there was a tear, but they do note a thickening of the Wadati–Benioff zone around ∼150 km. The lateral changes in deformation style revealed by our MT data set do indicate that a structure within the subducted Proto-Caribbean Plate may be present. The subducted domain boundary between plate material formed at the Proto-Caribbean (to the south) and Central Atlantic ridge (to the north) projects just north of the cluster (Fig. 10; magenta-red line), and part of the extinct Proto-Caribbean spreading ridge is expected to lie below the central arc (Fig. 13). A lateral variation in slab buoyancy (more buoyant in the south than north) might explain the along-strike variation in slab dip and introduce along-strike extensional stresses. However, the age, and hence negative buoyancy of the subducted plate increases southwards (Braszus *et al.* 2021; ∼30 Myr older in the south), although all of the plate is older than 70 Myr and hence age-related buoyancy gradients may be modest. On the other hand, a partial detachment of the southern end of the slab, along a lateral tear recognised at around 200 km depth below Grenada (Braszus *et al.* 2021), may be the cause of weaker slab pull in the south than in the north. Pre-existing

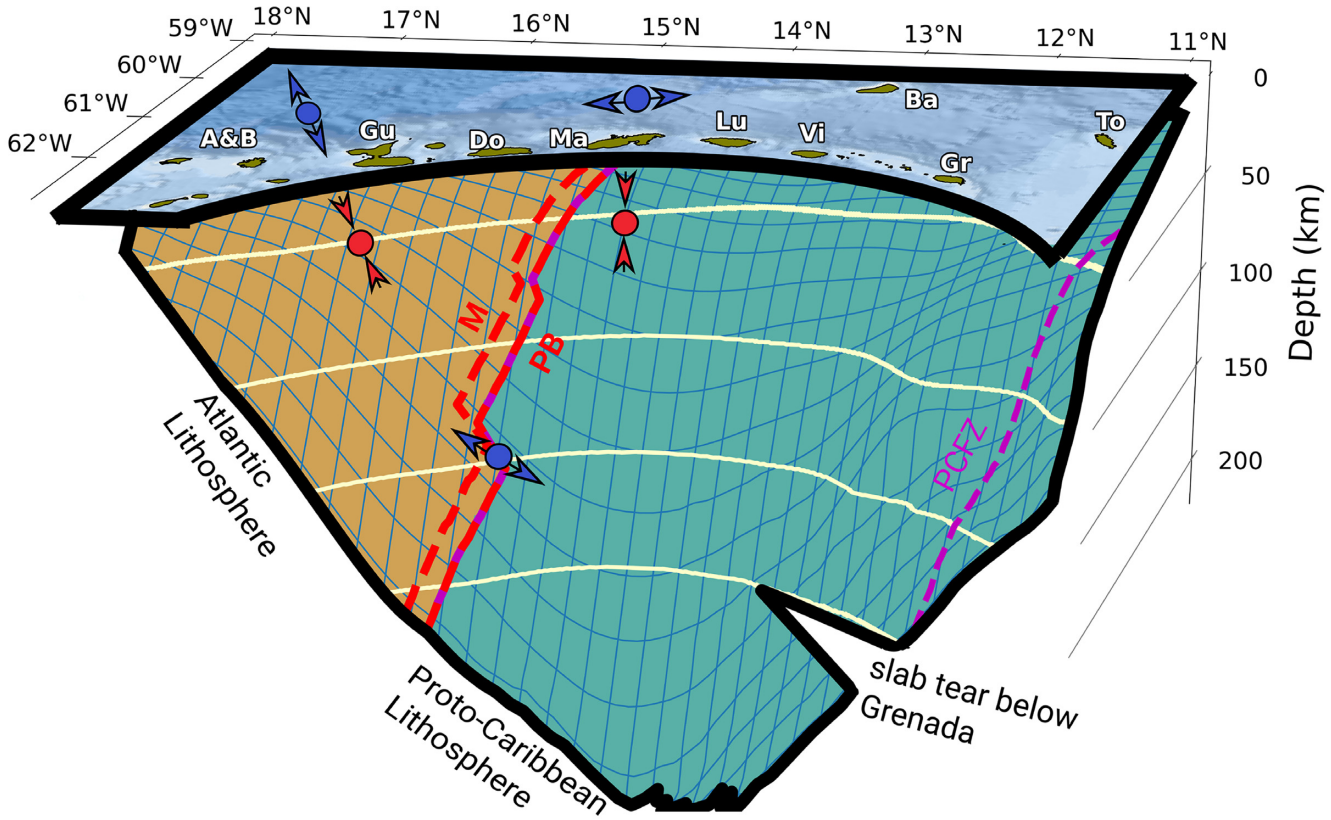

Figure 13. 3-D sketch of the Lesser Antilles subduction zone. Marked islands from north to south are Antigua and Barbuda (A&B), Guadalupe (GU), Dominica (Do), Martinique (Ma), St Lucia (Lu), St. Vincent (Vi), Barbados (Ba), Grenada (Gr) and Tobago (To). Outline of the slab is based on the local slab model by Bie *et al.* (2020) with spacial partition into Atlantic (brown) and Proto-Caribbean (green) lithosphere (Braszus *et al.* 2021). Relevant features are displayed in colour coding following Fig. 1 with M being the Marathon fracture zone, PB the plate boundary between the two lithospheres which also coincides with the Mercurius fracture zone and the unnamed Proto-Caribbean fracture zone PCFZ. Displayed arrows represent the dominant stress regime (red: compression, blue: extension), projected at the centroid location of the input data. The hypothesised lateral slab tear below Grenada is depicted at the depth outline of 200 km.

Proto-Caribbean structures in the downgoing plate may govern both the localisation of Wadati–Benioff seismicity in response to the stress regime due to along-strike slab pull variations, and the orientation of the seismically activated structures (Fig. 13).

7 CONCLUSIONS

We have developed a novel AmΦB-RMT approach which uses the uniXtree-sampling algorithm to mitigate the effects on RMT solutions from OBS data of uncertainties from horizontal station alignments and high levels of ocean microseisms. Our synthetic experiments show a reduction of the discrepancies between input and recovered CLVD percentage to be between 48 and 58 per cent compared to a classical L2 approach, depending on the number of stations used and the noise levels. We also observe a reduction in error in the recovered Kagan angle at large noise amplitudes, with up to 40 per cent improvement compared to a classical L2 approach. Inversions taking into account station alignment uncertainties at low noise are more robust if a model covariance matrix is included. Using only vertical traces it is possible and robust to solve in a double-couple inversion setup, as changes in CLVD are shown to mainly compensate for the effects of noise, but do not generally bias the retrieved planar fault geometry.

Application of our new method to the recorded OBS data of the VoiLA experiment in the LA subduction zone yields robust solutions as shown by the comparison with a teleseismically derived reference event set. We compiled 151 MT solutions, including 39 new ones from this study for the north-central LA arc and found 25 per cent normal faulting (NF), 25 per cent thrust faulting (TF), 10 per cent strike-slip faulting (SS) with the remainder being a mixture of mainly NF to SS transitional mechanisms. TF is dominant along the slab-upper-plate interface, with a notable gap in seismic activity between ∼15°N and ∼16.5°N. The general stress regime follows the subduction geometry of the slab. We find that the areas of interface activity coincide with the inferred rupture areas of the 1839 *M*7.5 and 1843 *M*8.5 megathrust events. Upper plate activity shows a strong variability along the arc. The north is characterized by a SS to NF transitional regime while the stress condition further south is dominantly an arc parallel extensional regime probably due to along-arc stretching of the forearc to accommodate the tight arc curvature. Stress inversion for an intermediate-depth central cluster offshore Martinique reflects downdip compression and slab-parallel extension. Downdip compression may reflect the dynamics of this relatively small subduction zone (van Benthem & Govers 2010), which has led to the piling of slab material within the upper mantle below the LA (Braszus *et al.* 2021). The along-strike extensional stress regime is unusual and we propose it to be due to lateral buoyancy variations, where pull at the southern end of the LA slab may be reduced by partial slab detachment along a lateral slab tear below Grenada (Braszus *et al.* 2021), causing slab deformation that localizes along pre-existing structures around the extinct Proto-Caribbean ridge subducted below Martinique (Fig. 13).

CODE AVAILABILITY

The moment tensor inversion code is available on GitHub at https://github.com/seismoMSL.

ACKNOWLEDGMENTS

This work was funded under Natural Environment Research Council (NERC) grant number NE/K010611/1. The authors thank the 'German Instrument Pool for Amphibian Seismology' (DEPAS AWI Bremerhaven & GFZ Potsdam) for providing the ocean-bottom seismometers and temporary island seismometers, and University of California, San Diego (UCSD) (Scripps) for providing additional ocean-bottom seismometers. The authors thank Carl Tape, Hannes Vasyura-Bathke and one anonymous reviewer for their helpful and constructive comments.

DATA AVAILABILITY

The data underlying this paper are available on the IRIS web service, at https://doi.org/10.7914/SN/XZ_2016.

REFERENCES

Aki, K. & Richards, P.G., 2002. *Quantitative Seismology,* 2nd edn, University Science Books.

Allen, R., Collier, J., Stewart, A., Henstock, T., Goes, S., Rietbrock, A. & the VoiLA Team, 2019. The role of arc migration in the development of the Lesser Antilles: a new tectonic model for the Cenozoic evolution of the eastern Caribbean, *Geology,* **47**(9), 891–895.

Alpert, L.A., Becker, T.W. & Bailey, I.W., 2010. Global slab deformation and centroid moment tensor constraints on viscosity, *Geochem. Geophys. Geosyst.,* **11**(12), doi:10.1029/2010GC003301.

Bailey, I.W., Alpert, L.A., Becker, T.W. & Miller, M.S., 2012. Co-seismic deformation of deep slabs based on summed CMT data, *J. geophys. Res.,* **117**(B4), doi:10.1029/2011JB008943.

Benthem, S., Govers, R., Spakman, W. & Wortel, R., 2013. Tectonic evolution and mantle structure of the Caribbean, *J. geophys. Res.,* **118,** 9200, doi:10.1002/jgrb.50235.

Bie, L. *et al.*, 2020. Along-arc heterogeneity in local seismicity across the Lesser Antilles subduction zone from a dense ocean-bottom seismometer network, *Seismol. Res. Lett.,* **91,** doi:10.1785/0220190147.

Bouysse, P., Westercamp, D. & Andreieff, P., 1990. The Lesser Antilles Island Arc 1, doi:10.2973/odp.proc.sr.110.166.1990.

Braszus, B. *et al.*, 2021. Subduction history of the Caribbean from upper-mantle seismic imaging and plate reconstruction, *Nat. Commun.,* **12**(1), 4211, doi:10.1038/s41467-021-24413-0.

Cabieces, R., Buforn, E., Cesca, S. & Pazos, A., 2020. Focal parameters of earthquakes offshore Cape St. Vincent using an amphibious network, *Pure appl. Geophys.,* **177** , doi:10.1007/s00024-020-02475-3.

Chen, P.-F., Bina, C.R. & Okal, E.A., 2004. A global survey of stress orientations in subducting slabs as revealed by intermediate-depth earthquakes, *Geophys. J. Int.,* **159**(2), 721–733.

Collier, J.S., 2015. VOILA - Volatile recycling in the Lesser Antilles arc: Leg 1, RRS James Cook JC133, 6-17 March 2016, Port of Spain, Trinidad-to-St Johns, Antigua, Imperial College London.

Cooper, G. *et al.*, 2020. Variable water input controls evolution of the Lesser Antilles Volcanic Arc, *Nature,* **582,** 525–529.

Dahm, T. & Krüger, F., 2014. Moment tensor inversion and moment tensor interpretation, in *New Manual of Seismological Observatory Practice 2 (NMSOP-2),* pp. 1–37, ed. Bormann, P., Deutsches GeoForschungsZentrum GFZ, doi:10.2312/GFZ.NMSOP-2_IS_3.9.

Delescluse, M., Montési, L. G.J. & Chamot-Rooke, N., 2008. Fault reactivation and selective abandonment in the oceanic lithosphere, *Geophys. Res. Lett.,* **35**(16) , doi:10.1029/2008GL035066.

Doran, A.K. & Laske, G., 2017. Ocean-bottom seismometer instrument orientations via automated rayleigh-wave arrival-angle measurement, *Bull. seism. Soc. Am.,* **107**(2), 691–708.

Duputel, Z., Rivera, L., Fukahata, Y. & Kanamori, H., 2012. Uncertainty estimations for seismic source inversions, *Geophys. J. Int.,* **190**(2), 1243–1256.

Duputel, Z., Agram, P.S., Simons, M., Minson, S.E. & Beck, J.L., 2014. Accounting for prediction uncertainty when inferring subsurface fault slip, *Geophys. J. Int.,* **197**(1), 464–482.

Feuillet, N., Manighetti, I., Tapponnier, P. & Jacques, E., 2002. Arc parallel extension and localization of volcanic complexes in Guadeloupe, Lesser Antilles, *J. geophys. Res.,* **107**(B12), ETG3–1-ETG3-29.

Feuillet, N., Beauducel, F., Jacques, E., Tapponnier, P., Delouis, B., Bazin, S., Vallée, M. & King, G.C.P., 2011a. The Mw = 6.3, November 21, 2004, Les Saintes earthquake (Guadeloupe): tectonic setting, slip model and static stress changes, *J. geophys. Res.,* **116**(B10), doi:10.1029/2011JB008310.

Feuillet, N., Beauducel, F. & Tapponnier, P., 2011b. Tectonic context of moderate to large historical earthquakes in the Lesser Antilles and mechanical coupling with volcanoes, *J. geophys. Res.,* **116,** doi:10.1029/2011JB008443.

Fujimura, K., Kunii, T., Yamaguchi, K. & Toriya, H., 1984. Octree-related data structures and algorithms, *IEEE Comp. Graph. Appl.,* **4**(01), 53–59.

Garth, T. & Rietbrock, A., 2014. Order of magnitude increase in subducted H_2O due to hydrated normal faults within the Wadati-Benioff zone, *Geology,* **42**(3), 207–210.

Gephart, J. & Forsyth, D., 1984. An improved method for determining the regional stress tensor using earthquake focal mechanism data: application to the San Fernando earthquake sequence, *J. geophys. Res.,* **89,** 2177–2180.

Giner-Robles, J., Perez-Lopez, R., Rodriguez-Pascua, M., Martinez-Diaz, J. & Gonzalez-Casado, J., 2009. Present-day strain field on the South American slab underneath the sandwich plate (Southern Atlantic Ocean): a kinematic model, *Geol. Soc. Lond. Spec. Publ.,* **328,** 155–167.

Goes, S., Agrusta, R., van Hunen, J. & Garel, F., 2017. Subduction-transition zone interaction: a review, *Geosphere,* **13**(3), 644–664.

Goes, S. *et al.*, 2019. Project VOILA: volatile recycling in the Lesser Antilles, *EOS, Trans. Am. geophys. Un.,* **100,** doi:10.1029/2019EO117309.

Gonzalez, O., Clouard, V. & Zahradník, J., 2017. Moment tensor solutions along the central Lesser Antilles using regional broadband stations, *Tectonophysics,* **717,** 214–225.

Harmon, N., Rychert, C., Collier, J., Henstock, T., van Hunen, J. & Wilkinson, J.J., 2019. Mapping geologic features onto subducted slabs, *Geophys. J. Int.,* **219**(2), 725–733.

Harris, C.W., Miller, M.S. & Porritt, R.W., 2018. Tomographic imaging of slab segmentation and deformation in the Greater Antilles, *Geochem. Geophys. Geosyst.,* **19**(8), 2292–2307.

Hayes, G.P., McNamara, D.E., Seidman, L. & Roger, J., 2013. Quantifying potential earthquake and tsunami hazard in the Lesser Antilles subduction zone of the Caribbean region, *Geophys. J. Int.,* **196**(1), 510–521.

Janiszewski, H.A. & Abers, G.A., 2015. Imaging the plate interface in the Cascadia Seismogenic Zone: new constraints from offshore receiver functions, *Seismol. Res. Lett.,* **86**(5), 1261–1269.

Jost, M. & Herrmann, R., 1989. A student's guide to and review of moment tensor, *Seismol. Res. Lett.,* **60**(2), 37–57.

Julien, P. & Bonneton, J.-R., 1989. Regional stress field in the Lesser Antilles between Guadeloupe and Barbuda islands, *Geophys. Res. Lett.,* **16**(11), 1313–1316.

Kagan, Y.Y., 1991. 3-D rotation of double-couple earthquake sources, *Geophys. J. Int.,* **106**(3), 709–716.

Krizova, D., Zahradnik, J. & Kiratzi, A., 2013. Resolvability of isotropic component in regional seismic moment tensor inversion, *Bull. seism. Soc. Am.,* **103,** 2460–2473.

Laigle, M., Becel, A., de Voogd, B., Sachpazi, M., Bayrakci, G., Jean-Frédéric, L. & Evain, M., 2013a. Along-arc segmentation and interaction of subducting ridges with the Lesser Antilles subduction forearc crust revealed by MCS imaging, *Tectonophysics,* **603,** 32–54.

Laigle, M. *et al.*, 2013b. Seismic structure and activity of the north-central Lesser Antilles subduction zone from an integrated approach: similarities with the tohoku forearc, *Tectonophysics,* **603,** 1–20.

Laurencin, M., Marcaillou, B., Graindorge, D., Klingelhoefer, F., Lallemand, S., Laigle, M. & Jean-Frédéric, L., 2017. The polyphased tectonic evolution of the anegada passage in the northern Lesser Antilles subduction zone, *Tectonics,* **36,** doi:10.1002/2017TC004511.

Lecocq, T. *et al.*, 2020. Global quieting of high-frequency seismic noise due to COVID-19 pandemic lockdown measures, *Science,* **369**(6509), 1338–1343.

León-Ríos, S. *et al.*, 2021. 3D local earthquake tomography of the WEcuadorian margin in the source area of the 2016 Mw 7.8 Pedernales earthquake, *J. geophys. Res.,* **126**(3), e2020JB020701, doi:10.1029/2020JB020701.

Lim, H., Kim, Y., Song, T.-R.A. & Shen, X., 2017. Measurement of seismometer orientation using the tangential P-wave receiver function based on harmonic decomposition, *Geophys. J. Int.,* **212**(3), 1747–1765.

Lomax, A. & Curtis, A., 2001. Fast, probabilistic earthquake location in 3D models using Oct-Tree importance sampling, European Geophysical Society, Nice.

Lund, B. & Townend, J., 2007. Calculating horizontal stress orientations with full or partial knowledge of the tectonic stress tensor, *Geophys. J. Int.,* **170**(3), 1328–1335.

Álvarez ómez, J.A., 2019. FMC—earthquake focal mechanisms data management, cluster and classification, *SoftwareX,* **9,** 299–307.

McCann, W.R. & Sykes, L.R., 1984. Subduction of aseismic ridges beneath the Caribbean Plate: implications for the tectonics and seismic potential of the northeastern Caribbean, *J. geophys. Res.,* **89**(B6), 4493–4519.

Meagher, D., 1982. The octree encoding method for efficient solid modeling, Technical rept., Accession Number: ADA132472.

Melekhova, E., Schlaphorst, D., Blundy, J., Kendall, J.-M., Connolly, C., McCarthy, A. & Arculus, R., 2019. Lateral variation in crustal structure along the Lesser Antilles arc from petrology of crustal xenoliths and seismic receiver functions, *Earth planet. Sci. Lett.,* **516,** 12–24.

Michael, A.J., 1984. Determination of stress from slip data: faults and folds, *J. geophys. Res.,* **89**(B13), 11 517–11 526.

Okuwaki, R., Hicks, S.P., Craig, T.J., Fan, W., Goes, S., Wright, T.J. & Yagi, Y., 2021. Illuminating a contorted slab with a complex intraslab rupture evolution during the 2021 Mw 7.3 East Cape, New Zealand earthquake, *Geophys. Res. Lett.,* **48**(24), e2021GL095117, doi:10.1029/2021GL095117.

Patriat, M., Pichot, T., Westbrook, G., Umber, M., Deville, E., Bénard, F., Roest, W. & Loubrieu, B., the ANTIPLAC Cruise Party, 2011. Evidence for Quaternary convergence across the North America–South America plate boundary zone, east of the Lesser Antilles, *Geology,* **39**(10), 979–982.

Paulatto, M., Laigle, M., Galve, A., Charvis, P., Sapin, M., Bayrakci, G., Evain, M. & Kopp, H., 2017. Dehydration of subducting slow-spread oceanic lithosphere in the Lesser Antilles, *Nat. Commun.,* **8,** doi:10.1038/ncomms15980.

Plenefisch, T., 1996. Untersuchungen des Spannungsfeldes im Bereich des Rheingrabens mittels der Inversion von Herdflaechenloesungen und Abschaetzung der bruchspezifischen Reibungsparameter, *Dissertation*, University of Kalrsuhe.

Plenefisch, T. & Bonjer, K.-P., 1997. The stress field in the Rhine Graben Area inferred from earthquake focal mechanisms and estimation of frictional parameters, *Tectonophysics,* **275**(1), 71–97.

Pugh, D.J., White, R.S. & Christie, P. A.F., 2016. A Bayesian method for microseismic source inversion, *Geophys. J. Int.,* **206**(2), 1009–1038.

Ringler, A.T., Hutt, C.R., Persefield, K. & Gee, L.S., 2013. Seismic station installation orientation errors at ANSS and IRIS/USGS stations, *Seismol. Res. Lett.,* **84**(6), 926–931.

Romanowicz, B. *et al.*, 1998. Moise: a pilot experiment towards long term sea-floor geophysical observatories, *Earth Planets Space,* **50,** 927–937.

Rontogianni, S., Konstantinou, K., Melis, N. & Evangelidis, C., 2010. Slab stress field in the Hellenic subduction zone as inferred from intermediate depth earthquakes, *AGU Fall Meeting Abstracts,* **63,** doi:10.5047/eps.2010.11.011.

Ruiz, M. *et al.*, 2013. Seismic activity offshore martinique and Dominica islands (central Lesser Antilles subduction zone) from temporary onshore and offshore seismic networks, *Tectonophysics,* **603,** 68–78.

Schlaphorst, D. *et al.*, 2016. Water, oceanic fracture zones and the lubrication of subducting plate boundaries—insights from seismicity, *Geophys. J. Int.,* **204**(3), 1405–1420.

Schlaphorst, D., Kendall, J.-M., Baptie, B., Latchman, J.L. & Tait, S., 2017. Gaps, tears and seismic anisotropy around the subducting slabs of the Antilles, *Tectonophysics,* **698,** 65–78.

Sokos, E.N. & Zahradnik, J., 2008. Isola a Fortran code and a Matlab GUI to perform multiple-point source inversion of seismic data, *Comput. Geosci.,* **34**(8), 967–977.

Sokos, E.N. & Zahradnik, J., 2013. Evaluating centroid-moment-tensor uncertainty in the new version of Isola software, *Seismol. Res. Lett.,* **84,** 656–665.

Staehler, S. & Sigloch, K., 2014. Fully probabilistic seismic source inversion – part 1: efficient parameterisation, *Solid Earth,* **5,** 1055–1069.

Tape, W. & Tape, C., 2015. A uniform parametrization of moment tensors, *Geophys. J. Int.,* **202**(3), 2074–2081.

Tape, W. & Tape, C., 2016. A confidence parameter for seismic moment tensors, *Geophys. J. Int.,* **205**(2), 938–953.

Tashiro, Y., 1977. On methods for generating uniform random points on the surface of a sphere., *Ann Inst Stat Math,* **29,** 295–300.

Trabattoni, A., Barruol, G., Dreo, R., Boudraa, A.-O. & Fontaine, F., 2020. Orienting and locating ocean-bottom seismometers from ship noise analysis, *Geophys. J. Int.,* **220,** 1774–1790.

Vackář, J., Burjánek, J., Gallovič, F., Zahradík, J. & Clinton, J., 2017. Bayesian ISOLA: new tool for automated centroid moment tensor inversion, *Geophys. J. Int.,* **210**(2), 693–705.

van Benthem, S. & Govers, R., 2010. The Caribbean plate: pulled, pushed, or dragged?, *J. geophys. Res.,* **115**(B10), doi:10.1029/2009JB006950.

van Rijsingen, E.M., Calais, E., Jolivet, R., de Chabalier, J.-B., Jara, J., Symithe, S., Robertson, R. & Ryan, G.A., 2021. Inferring interseismic coupling along the Lesser Antilles arc: a Bayesian approach, *J. geophys. Res.,* **126**(2), e2020JB020677, doi:10.1029/2020JB020677.

Vasyura-Bathke, H. *et al.*, 2020. The Bayesian earthquake analysis tool, *Seismol. Res. Lett.,* **91**(2A), 1003–1018.

Vasyura-Bathke, H., Dettmer, J., Dutta, R., Mai, P.M. & Jónsson, S., 2021. Accounting for theory errors with empirical Bayesian noise models in nonlinear centroid moment tensor estimation, *Geophys. J. Int.,* **225**(2), 1412–1431.

Vavryvcuk, V., 2014. Iterative joint inversion for stress and fault orientations from focal mechanisms, *Geophys. J. Int.,* **199,** 69–77.

Wang, P.-S., Liu, Y., Guo, Y.-X., Sun, C.-Y. & Tong, X., 2017. O-cnn: Octree-based convolutional neural networks for 3D shape analysis, *ACM Trans. Graph.,* **36**(4), doi:10.1145/3072959.3073608.

Wang, X., Chen, Q.-f., Li, J. & Wei, S., 2016. Seismic sensor misorientation measurement using p-wave particle motion: an application to the Necsaids array, *Seismol. Res. Lett.,* **87,** 901–911.

Yagi, Y. & Fukahata, Y., 2008. Importance of covariance components in inversion analyses of densely sampled observed data: an application to waveform data inversion for seismic source processes, *Geophys. J. Int.,* **175**(1), 215–221.

Yang, Z., Sheehan, A.F., Collins, J.A. & Laske, G., 2012. The character of seafloor ambient noise recorded offshore New Zealand: results from the moana ocean bottom seismic experiment, *Geochem. Geophys. Geosyst.,* **13**(10), doi:10.1029/2012GC004201.

Zha, Y., Webb, S.C. & Menke, W., 2013. Determining the orientations of ocean bottom seismometers using ambient noise correlation, *Geophys. Res. Lett.,* **40**(14), 3585–3590.

Zhao, L.-S. & Helmberger, D.V., 1994. Source estimation from broadband regional seismograms, *Bull. seism. Soc. Am.,* **84**(1), 91–104.

Zhu, L. & Ben-Zion, Y., 2013. Parametrization of general seismic potency and moment tensors for source inversion of seismic waveform data, *Geophys. J. Int.,* **194**(2), 839–843.